DOE/BC/14897-6
Distribution Category UC-122

Anisotropy and Spatial Variation of Relative Permeability and Lithologic Character of Tensleep Sandstone Reservoirs in the Bighorn and Wind River Basins, Wyoming

Annual Report for the Period
September 15, 1993 to September 30, 1994

By
Thomas L. Dunn

July 1995

Work Performed Under Contract No. DE-AC22-93BC14897

Prepared for
U.S. Department of Energy
Assistant Secretary for Fossil Energy

R.E. Lemmon, Project Manager
Bartlesville Project Office
P.O. Box 1398
Bartlesville, OK 74005

MASTER

Prepared by
University of Wyoming
Laramie, Wyoming

DISTRIBUTION OF THIS DOCUMENT IS UNLIMITED

DISCLAIMER

This report was prepared as an account of work sponsored by an agency of the United States Government. Neither the United States Government nor any agency thereof, nor any of their employees, makes any warranty, express or implied, or assumes any legal liability or responsibility for the accuracy, completeness, or usefulness of any information, apparatus, product, or process disclosed, or represents that its use would not infringe privately owned rights. Reference herein to any specific commercial product, process, or service by trade name, trademark, manufacturer, or otherwise does not necessarily constitute or imply its endorsement, recommendation, or favoring by the United States Government or any agency thereof. The views and opinions of authors expressed herein do not necessarily state or reflect those of the United States Government or any agency thereof.

DISCLAIMER

Portions of this document may be illegible in electronic image products. Images are produced from the best available original document.

TABLE OF CONTENTS

List of Figures

Task 1.0

Task 2.0

Task 3.0

Task 4.0

List of Tables

Task 1.0

Task 2.0

Task 3.0

EXECUTIVE SUMMARY

Background

Permeability variations in reservoirs include the spatial variation (heterogeneity) of absolute and relative permeability and the directional variation (anisotropy) of absolute and relative permeability. Absolute permeability has been extensively studied by other research teams in academia and the petroleum industry. However, relative permeability anisotropy and spatial variations have yet to be considered as to the effects on oil and gas production. The principal focus of this project is to evaluate the importance of relative permeability anisotropy with respect to other known geologic and engineering production concepts.

This research is to provide improved strategies for enhanced oil recovery from the Tensleep Sandstone oil reservoirs in the Bighorn and Wind River basins, Wyoming. The Tensleep Sandstone contains the largest potential reserves within reservoirs which are candidates for EOR processes in the State of Wyoming. Although this formation has produced billions of barrels of oil, in some fields, as little as one in seven barrels of discovered oil is recoverable by current primary and secondary techniques. Because of the great range of °API gravities of the oils produced from the Tensleep Sandstone reservoirs, the proposed study concentrates on establishing an understanding of the spatial variation and anisotropy of relative permeability within the Tensleep Sandstone. This research is to associate those spatial distributions and anisotropies with the depositional subfacies and zones of diagenetic alteration found within the Tensleep Sandstone.

The associations between depositional lithofacies, diagenetic alteration, and pore geometry will strongly link relative permeability with the distinct and measurable dimensions of lithofacies and authigenic mineral facies. Hence, the study is to provide criteria for scaling this parameter on a range of scales — from the volume of laboratory investigation to the basin-wide scale of subfacies distribution. Effects of both the depositional processes and the burial diagenesis will be investigated. Image analysis of pore systems will be performed so as to produce algorithms for estimating relative permeability from petrographic analyses of core and well cuttings.

In addition, these studies are being coupled with geochemical modeling and coreflood experiments to investigate the potential for wellbore scaling and formation damage anticipated during EOR processes (e.g., CO_2 flooding). This multidisciplinary project will provide a regional basis for EOR strategies which can be clearly mapped and efficiently applied to the largest potential target reservoir in the State of Wyoming. Additionally, the results of this study have application to all eolian reservoirs through the correlations of relative permeability variation and anisotropy with eolian depositional lithofacies.

Results

The first year of the project has included the efforts of eleven individuals working on three research tasks and one administrative task. Discussions of the accomplishments of each of the tasks can be found in the sections which follow. There are four main points which the work has demonstrated:

1) We have applied a process-oriented approach to the subdivision and examination of the internal fabric present in the Tensleep. The characterization of the internal fabrics and bounding surfaces can be placed in a regional context using this basic approach.

2) We have observed relative permeability anisotropy in the first sets of samples measured using the relative permeameter which we have constructed and tested.

3) We have successfully completed a CO_2 coreflood experiment which simulates insitu conditions such that the behavior of the water chemistry evolution mimics that of observed trends from CO_2 field tests performed in Tensleep reservoirs in Wyoming.

4) We have successfully put into place a multidisciplinary team of scientists with a wide range of industry and research experience. The project enjoys continued support of the State and of the petroleum industry.

TASK 1.0 - REGIONAL FRAMEWORKS.

OBJECTIVES

This research will associate spatial distributions and anisotropy of relative permeability with the depositional subfacies and zones of diagenetic alteration found within the Tensleep Sandstone. The associations between depositional lithofacies diagenetic alteration, and pore geometry will link relative permeability with the distinct and measurable dimensions of lithofacies, and authigenic mineral facies. Effects of the depositional processes and burial diagenesis will be investigated.

INTRODUCTION

The primary goal of this task is to establish the regional trends and variations in lithologic character of the eolian and marine subfacies of the upper Tensleep Sandstone in the Bighorn and Wind River basins. This work is being accomplished through field work, examination of subsurface cores, and the construction and analysis of a regional database utilizing well log data and core analysis. The surface and subsurface data that has been gathered indicate that the depositional fabric of the rocks controls the spatial variation of permeability. We are applying the concepts of preservation and accumulation space as a basis for characterizing the regional variation of lithofacies in the Tensleep Formation. The processes that controlled accumulation versus preservation of the upper Tensleep Sandstone in the Bighorn Basin are distinct, and as such have produced different internal fabrics and bounding surfaces which affect reservoir heterogeneity. Accumulation is the short-term net deposition of sediments within an eolian system, whereas preservation marks the entrance of the sediments into the stratigraphic record (Fig. 1).

Work to date has concentrated on establishing a comprehensive database of well logs, core, and outcrop description. As of September 30, 1994, 173 well logs and 61 core analyses had been digitized and entered into the Production Analyst© database for both the Bighorn and Wind River basins (Figs. 2 and 3). This database includes 7,000 feet of core analyses and 32,000 feet each of the digitized well logs (GR, Neu, Den) for the Bighorn

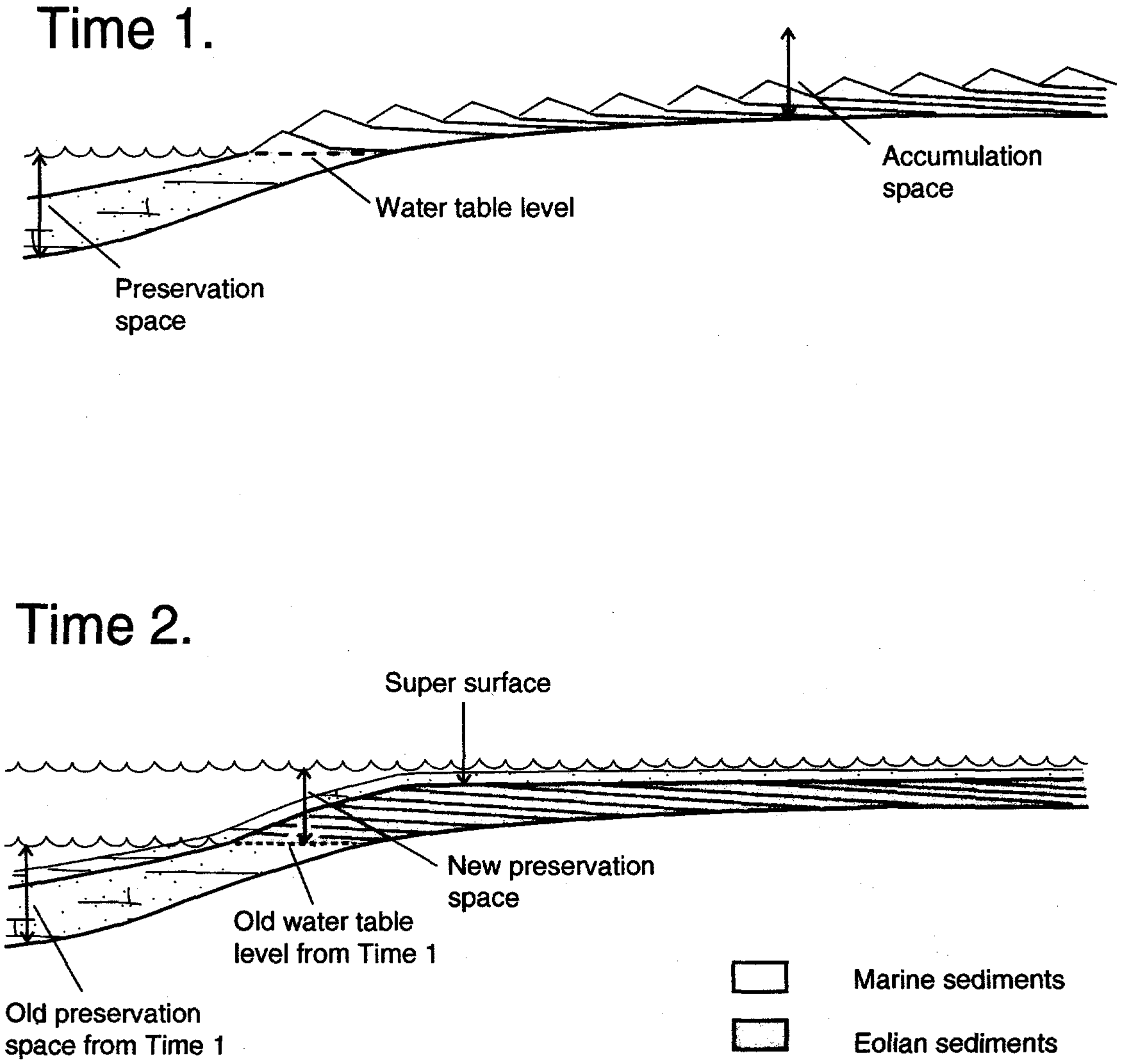

Figure 1. Examples illustrating the difference between accumulation in a dry eolian system (Time 1) and preservation of an eolian accumulation under the influence of a relatively rising water table (Time 2). Modified from Kocurek and Havholm, 1993.

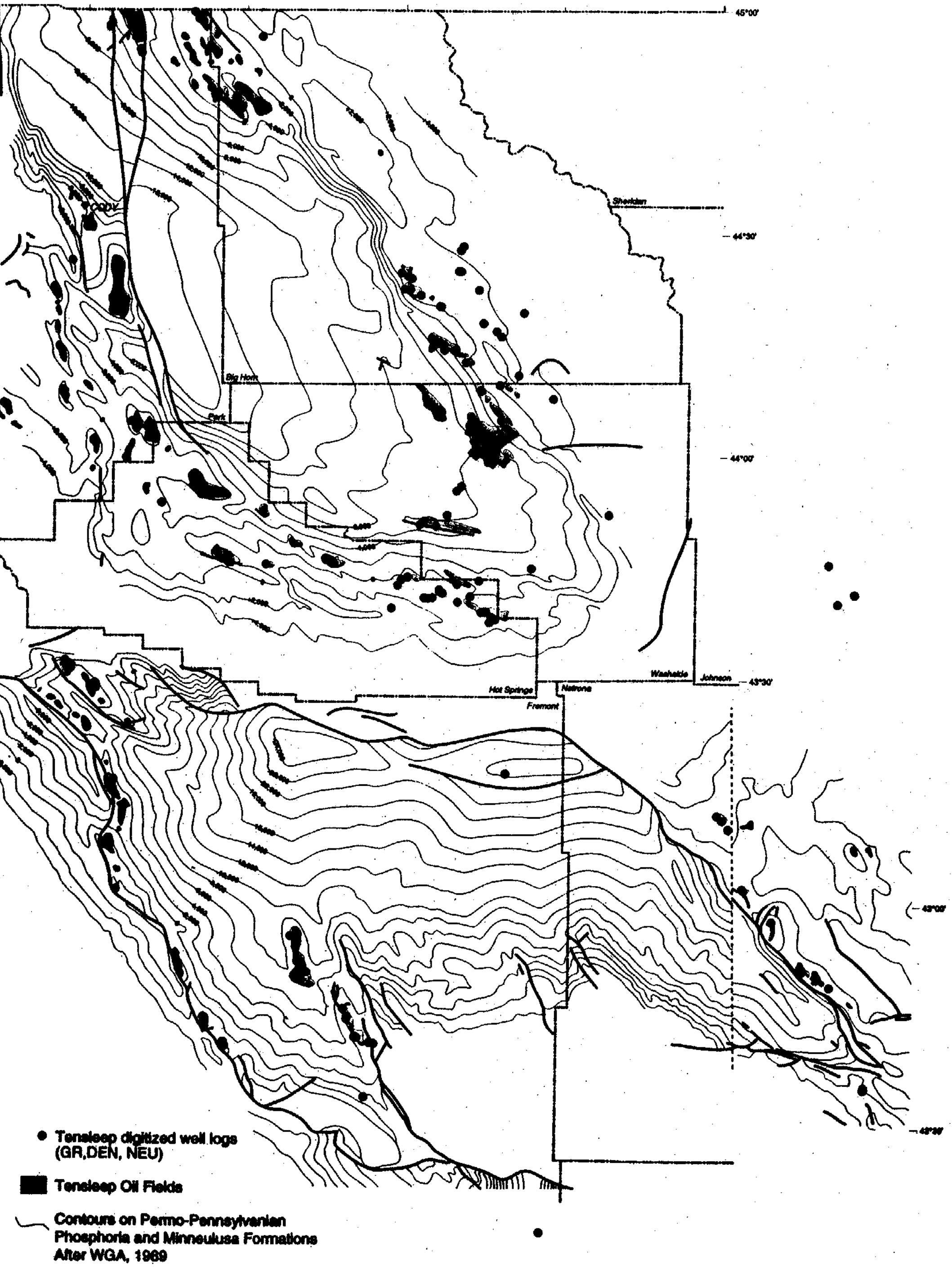

Figure 2. Location of Tensleep oil fields and digitized well log for the Bighorn and Wind River basins as of September 30, 1994.

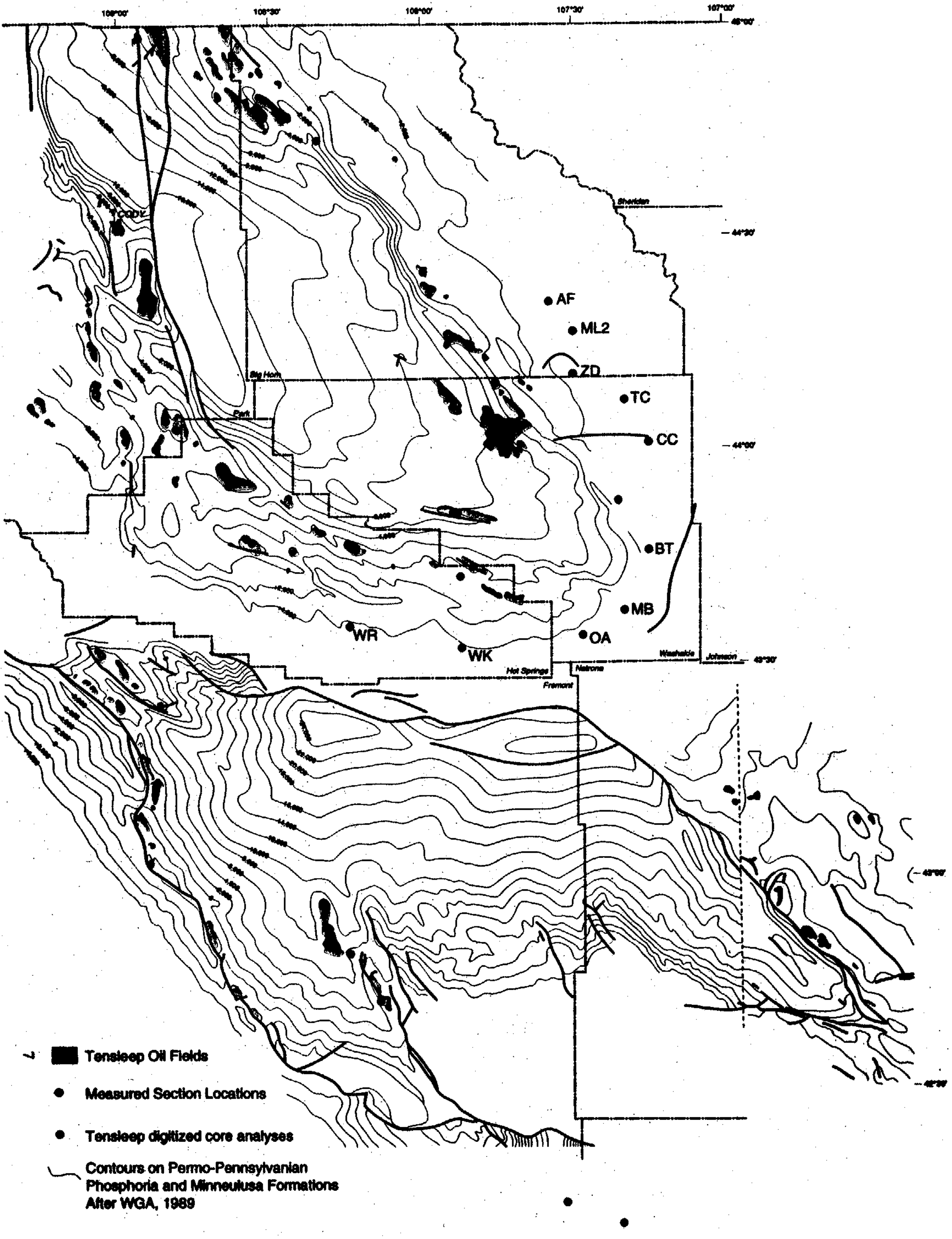
109°00'
108°30'
108°00'
107°30'
107°00'
45°00'
44°30'
44°00'
43°30'
43°00'
42°30'
Sheridan
Big Horn
Park
Washakie
Johnson
Hot Springs
Natrona
Fremont
CODY
AF
ML2
ZD
TC
CC
BT
MB
OA
WR
WK
Tensleep Oil Fields
Measured Section Locations
Tensleep digitized core analyses
Contours on Permo-Pennsylvanian Phosphoria and Minneulusa Formations After WGA, 1989

Basin, and 1,500 feet of core analyses and 22,000 feet each of the well log data for the Wind River Basin. Field studies (37 days of a 2 person field party) have concentrated on the southeastern portion of the Bighorn Basin where eight vertical sections have been measured and a series of sixteen photomosaics have been constructed illustrating the scales of reservoir heterogeneity, which exist in the Tensleep (Fig. 3). These data indicate that the Tensleep Sandstone can readily be divided into a series of eolian sandstone and marine dolomite cycles. These cycles have been related to regressive-transgressive cycles as illustrated in Figure 4 (Andrews and Higgins, 1984; Wheeler, 1986; and Kerr, 1989). These cycles have created large-scale boundaries to reservoir continuity and influence horizontal and vertical sweep efficiency.

Samples have been taken from outcrop locations as well as from two cores for use in core flood and relative permeability studies undertaken in Tasks 2 and 3. Tables 1 and 2 indicate the nature of cross-strata from which the samples were taken as well as the orientation of the samples. These samples represent key lithofacies and cementation patterns observed in the Tensleep. Thin sections have also been prepared from all of the samples.

Accumulation and Preservation

Understanding the different scales of reservoir heterogeneity is greatly enhanced by developing an understanding of the dynamics of the eolian systems that produced these reservoir rocks. Accumulation of the upper Tensleep Sandstone in the Bighorn Basin occurred within a dry eolian system, that is one in which accumulation occurs as a result of aerodynamic controls, and is unaffected by the local water table. Conversely, preservation of the upper Tensleep was caused by the relative rise of sea level that placed the area below the regional baseline of erosion. The orientation and character of the bounding surfaces and internal laminations of eolian facies in the Tensleep indicate that the ergs were

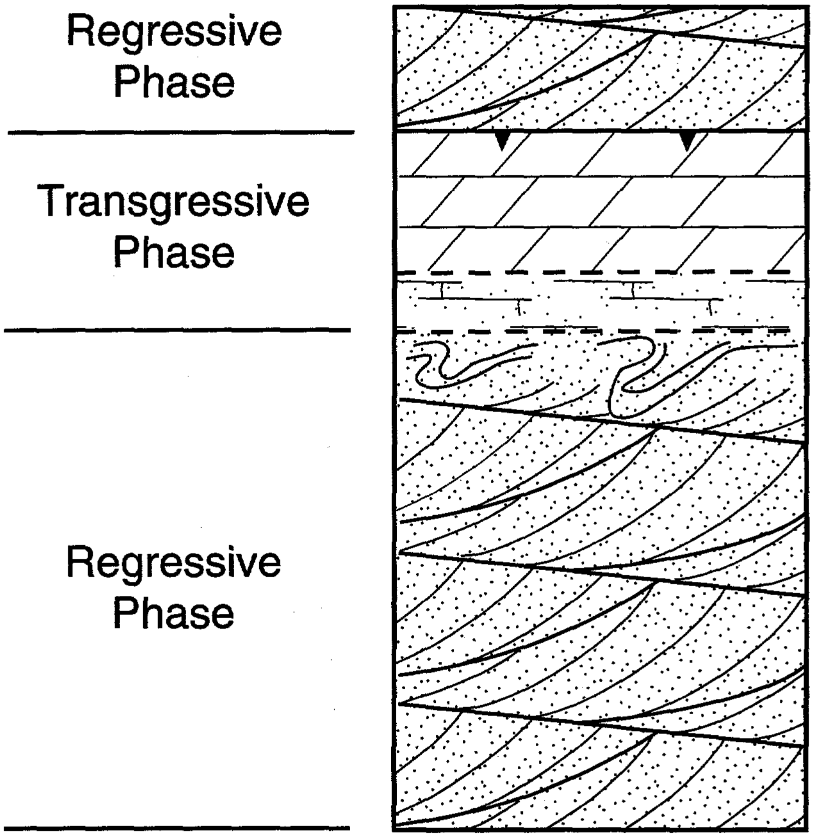

Figure 4. Idealized eolian-marine cycle and its relationship to sea-level change.

Table 1. Samples taken for relative permeability studies associated with Task 2.0.

Sample	Core Orientation		Stratification	Location Name
Ah	horizontal		wind ripple	Ziesman Dome
Av	vertical		wind ripple	Ziesman Dome
Bh	horizontal		wind ripple	Tensleep Canyon
Bv	vertical		wind ripple	Tensleep Canyon
Ch1	horizontal	130°	wind ripple?	Mahogany Butte
Ch2	horizontal	220°	wind ripple?	Mahogany Butte
Cv	vertical		wind ripple?	Mahogany Butte
Dh1	horizontal	65°	wind ripple	Mahogany Butte
Dh2	horizontal	175°	wind ripple	Mahogany Butte
Dh3	horizontal	175°	grainflow	Mahogany Butte
Dv	vertical		wind ripple	Mahogany Butte
Eh1	horizontal		grainflow	Mahogany Butte
Eh2	horizontal		wind ripple	Mahogany Butte
Ev	vertical		wind ripple	Mahogany Butte
Fh	horizontal		wind ripple	Canyon Creek
Fv	vertical		grainflow	Canyon Creek
Gh1	horizontal	180°	wind ripple	Upper Crooked Creek
Gh2	horizontal	270°	wind ripple	Upper Crooked Creek
Gv	vertical		wind ripple	Upper Crooked Creek
Hh1	horizontal	50°	wind ripple	Rome Hill Rd
Hh2	horizontal	350°	wind ripple	Rome Hill Rd
Hv	vertical		wind ripple	Rome Hill Rd
Ih1	horizontal	215°	WR/grainflow	6 miles Mayworth
Ih2	horizontal	260°	WR/grainflow	6 miles Mayworth
Iv	vertical		WR/grainflow	6 miles Mayworth

Table 2. List of samples from subsurface cores used in Tasks 2 and 3.

Gov't Tract 3B #8 Sample	Depth	Sample Orientation	Stratification
1	3217'	parallel to bedding	wind ripple laminae
2	3217' 2"	horizontal	wind ripple laminae
3	3217' 6"	parallel to bedding	wind ripple laminae
4	3240'	parallel to bedding	wind ripple laminae
5	3240' 5"	parallel to bedding	wind ripple laminae
6	3242' 1.5"	horizontal	wind ripple laminae
7	3242' 3"	horizontal	wind ripple laminae
8	3242' 5"	horizontal	wind ripple laminae
9	3242' 7"	horizontal	wind ripple laminae
10	3247' 10"	vertical	wind ripple laminae
11	3248' 2"	horizontal	wind ripple laminae
12	3286' 7"	parallel to bedding	wind ripple laminae
13	3287' 1"	parallel to bedding	wind ripple laminae
14	3287' 3.5"	parallel to bedding	wind ripple laminae
15	3287' 9"	parallel to bedding	wind ripple laminae
16	3288'	parallel to bedding	wind ripple laminae
17	3288' 3"	parallel to bedding	wind ripple laminae
18	3288' 9"	vertical	wind ripple laminae
19	3289' 6.5"	horizontal	wind ripple laminae

Marathon Wison B-12 Sample	Depth	Sample Orientation	Stratification
20	4013' 7"	vertical	wind ripple laminae
21	4014' 1"	horizontal	wind ripple laminae
22	3985' 10"	vertical	wind ripple laminae
23	3986'	parallel to bedding	wind ripple laminae
24	3986' 3"	parallel to bedding	wind ripple laminae
25	3986' 5"	parallel to bedding	wind ripple laminae
26	3979' 1"	horizontal	wind ripple laminae
27	3979' 6"	vertical	wind ripple laminae
28	3979' 10.5"	parallel to bedding	wind ripple laminae
29	3962' 1"	parallel to bedding	disturbed wr laminae
30	3961' 11"	vertical	disturbed wr laminae
31	3962' 3"	parallel to bedding	disturbed wr laminae
32	3962' 8"	parallel to bedding	disturbed wr laminae
33	3962 10"	parallel to bedding	disturbed wr laminae
34	3963'	parallel to bedding	disturbed wr laminae
35	3963' 2"	parallel to bedding	disturbed wr laminae

dominated by large compound bedforms that were affected by annual fluctuations in airflow.

Reservoir heterogeneity can be considered on a number of scales within the upper Tensleep Sandstone. Small-scale heterogeneities, such as internal bounding surfaces and lateral variations in microscopic pore structure, are the result of variations in the character of the bedforms during accumulation. These variations in internal fabric, along with drive type and fluid mobility ratio, govern sweep efficiency and ultimate recovery. Large-scale heterogeneities, represented by the areally extensive bedded dolomites within the upper Tensleep, are controlled by the longer term variations in preservation space as influenced by relative sea level fluctuations. These features govern overall reservoir continuity and, along with tectonic fabric, reservoir size.

Accumulation in most eolian systems occurs above some regional baseline of erosion (Fig. 1), and for this reason the controls on accumulation versus preservation in the rock record can be considered as distinct (Kocurek and Havholm, 1993). Accumulation is defined as "net deposition through time such that a three-dimensional body of strata is formed, and as such is distinct from deposition in that the later refers to the instantaneous net transfer of sediment from transport to the substrate" (Kocurek and Havholm, 1993). Preservation refers to the placing of an accumulation below some regional baseline of erosion. The Tensleep represents a depositional system in which accumulation and preservation of the eolian sediments occur independently under the influence of separate controls.

Kocurek and Havholm (1993) identified a spectrum of eolian systems as dry, wet and stabilized depending on the geological processes affecting accumulation. Study of Tensleep Sandstone outcrops in the southeastern Bighorn Basin indicates that the cross-stratified facies of the Tensleep Sandstone accumulated within a dry eolian system. In a dry eolian system the water table is at a depth below the sediment surface such that it has no stabilizing influence on the sediment, and therefore accumulation in a dry eolian system takes place strictly for aerodynamic reasons (Kocurek and Havholm, 1993). Studies of airflow over dunes and interdune areas indicate much of the interdune area is marked by flow acceleration and as such is potentially erosional (Frank, 1994). For this reason accumulation in a dry eolian system is unlikely to occur until the interdune areas have been eliminated by dune growth. Therefore, dry eolian systems such as the Tensleep are characterized by a paucity or lack of interdune accumulations.

PALEOGEOGRAPHIC AND PALEOCLIMATIC SETTING

The Tensleep Sandstone is Middle Pennsylvanian (Desmoinesian) to Lower Permian (Wolfcampian) in age based primarily on fusulinids (Branson, 1939; Henbest, 1954, 1956; and Verville, 1957) and corroborated by brachiopod (Brainerd and Keyte, 1927; Hoare and Burgess, 1960) and conodont studies (Rhodes, 1963) (Fig. 5). Verville et al., (1970) also demonstrated differential truncation of the Tensleep along the eastern flank of the southern Bighorn Mountains, with Wolfcampian strata exposed at the top of the Tensleep in southern areas and Desmoinesian strata exposed at the top in the northern areas.

Deposition and post-depositional erosion of the Tensleep Sandstone in southeastern Bighorn Basin was heavily influenced by the northeast-southwest trending Greybull Arch. Wheeler (1986) demonstrated thinning of caliche cycles within the Lower Tensleep onto this paleotopographic high. The progressive northward thinning of the Tensleep Sandstone in southeastern Bighorn Basin is attributed to post-Tensleep uplift of the Greybull Arch and corresponding increased rates of erosion, probably during Wolfcampian time (Agatston, 1954; Thomas, 1965; Mankiewicz and Steidtmann, 1979; Wheeler, 1986; Kerr et al., 1986; Kerr, 1989).

The Amsden-Tensleep sequence (Fig. 5) represents a transgressive-regressive cycle. The regressive portion represented by the Tensleep was punctuated by short-term transgressions represented by marine carbonate units (Mankiewicz and Steidtmann, 1979;

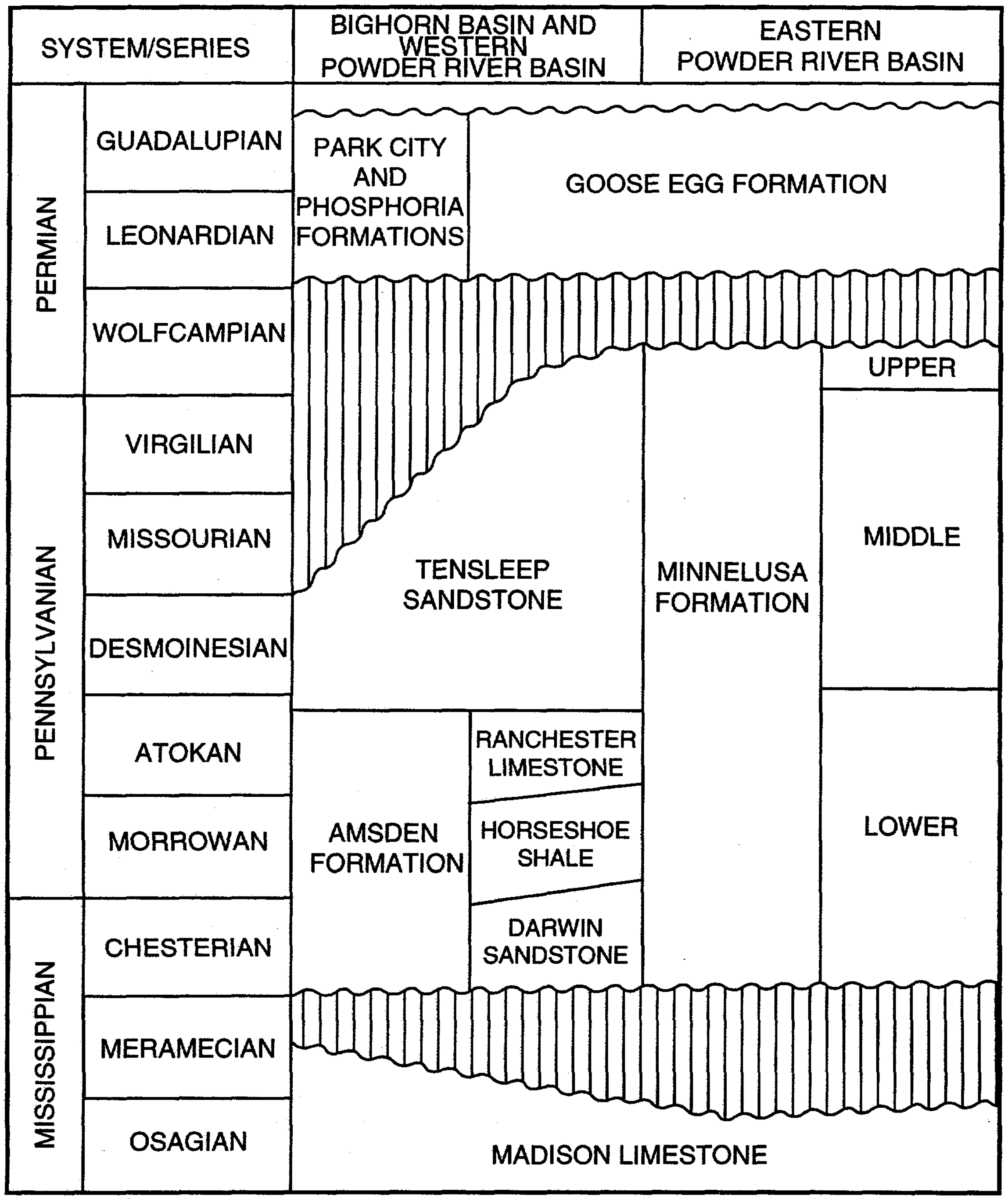

Figure 5. Correlation chart showing Mississippian throught Permian units in the Bighorn and Powder River basins (after Wheeler, 1986).

Andrews and Higgins,1984; Wheeler, 1986; Kerr, 1989). Wheeler (1986) considered the unconformity at the top of the Grandeur Member of the Park City Formation a second-order cycle correlating to the pre-middle-Leonardian sea-level drop of Vail et al. (1977). Wheeler (1986) further related eolian-marine cycles in the Tensleep to third- and fourth-order cycles resulting from glaciation in the southern hemisphere (Wanless and Shepard, 1936; Crowell and Frakes, 1972; Ramsbottom, 1979).

Figure 6 illustrates the general paleogeography for the Late Pennsylvanian to Early Permian during sea level lowstand. The study area was at approximately 10° north latitude during accumulation of the Tensleep Sandstone (Scotese et al., 1979). Paleocurrent measurements from eolian cross-strata indicate a predominance of southwest dips. This corresponds well with paleowindflow reconstructions for this time period shown in Figure 6 that indicate it was dominated by north to northeasterly winds (Parrish and Peterson, 1988; Peterson, 1988). The global circulation models of Parrish and Peterson (1988) also indicate annual fluctuations in wind direction such that the summer winds were northerly and the winter winds were northeasterly.

DEPOSITIONAL LITHOFACIES

Following the method of Agatston (1952, 1954) and Wheeler (1986) the Tensleep has been informally divided into lower and upper units using the top of a widespread fusulinid, coral-bearing, dolomitic sandstone. This is also approximately equivalent to the division proposed by Mankiewicz and Steidtmann (1979). This sandstone is recognized in well logs as a high density, low porosity bed that separates the serrated well-log signature of the lower from the more blocky signature of the upper Tensleep (Fig. 7). Because this marker can be distinguished on well logs and correlated throughout the Bighorn Basin it will be used as the datum on all correlations for this study (Fig. 7) .

The lower Tensleep varies in thickness from 15 to 37 meters and is characterized by burrowed sandstones, thin cross-stratified sets and fossiliferous, dolomitic, sandstones. In

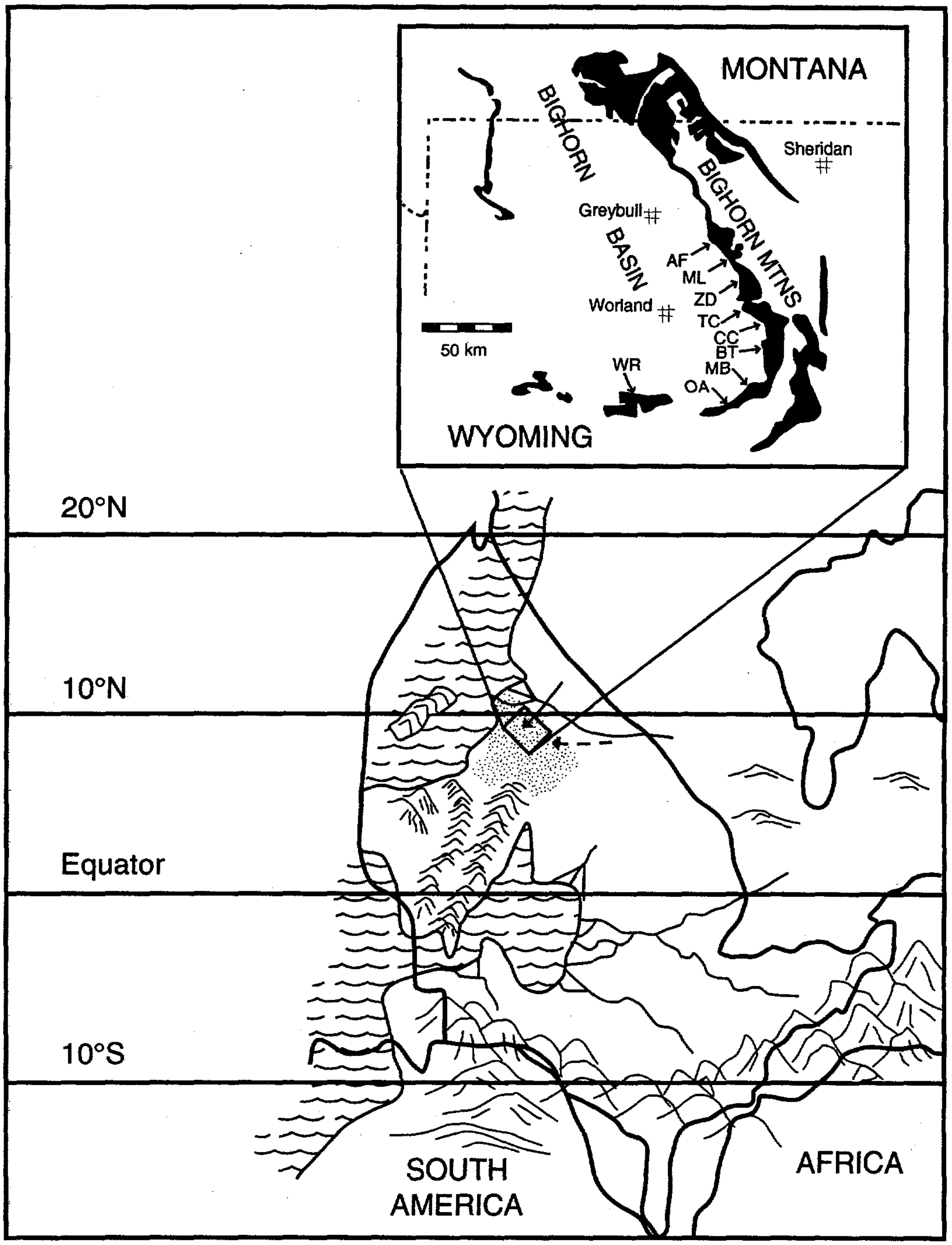

Figure 6. Generalized Pennsylvanian to Early Permian paleogeography during a low sea level stand. Stipple pattern equals eolian development. Inset map of north-central Wyoming showing outcrop pattern and vertical sections for this study (AF=Alkali Flats, ML=Medicine Lodge, ZD=Ziesman Dome, TC= Tensleep Canyon, CC= Canyon Creek, BT=Big Trails, MB=Mohagany Butte, OA=Orchard Anticline, WR=Wind River Canyon). Arrows depict paleowind directions from Parrish and Peterson (1988). Solid arrow is summer, dashed arrow is winter. Modified from Kerr and Dott, 1988.

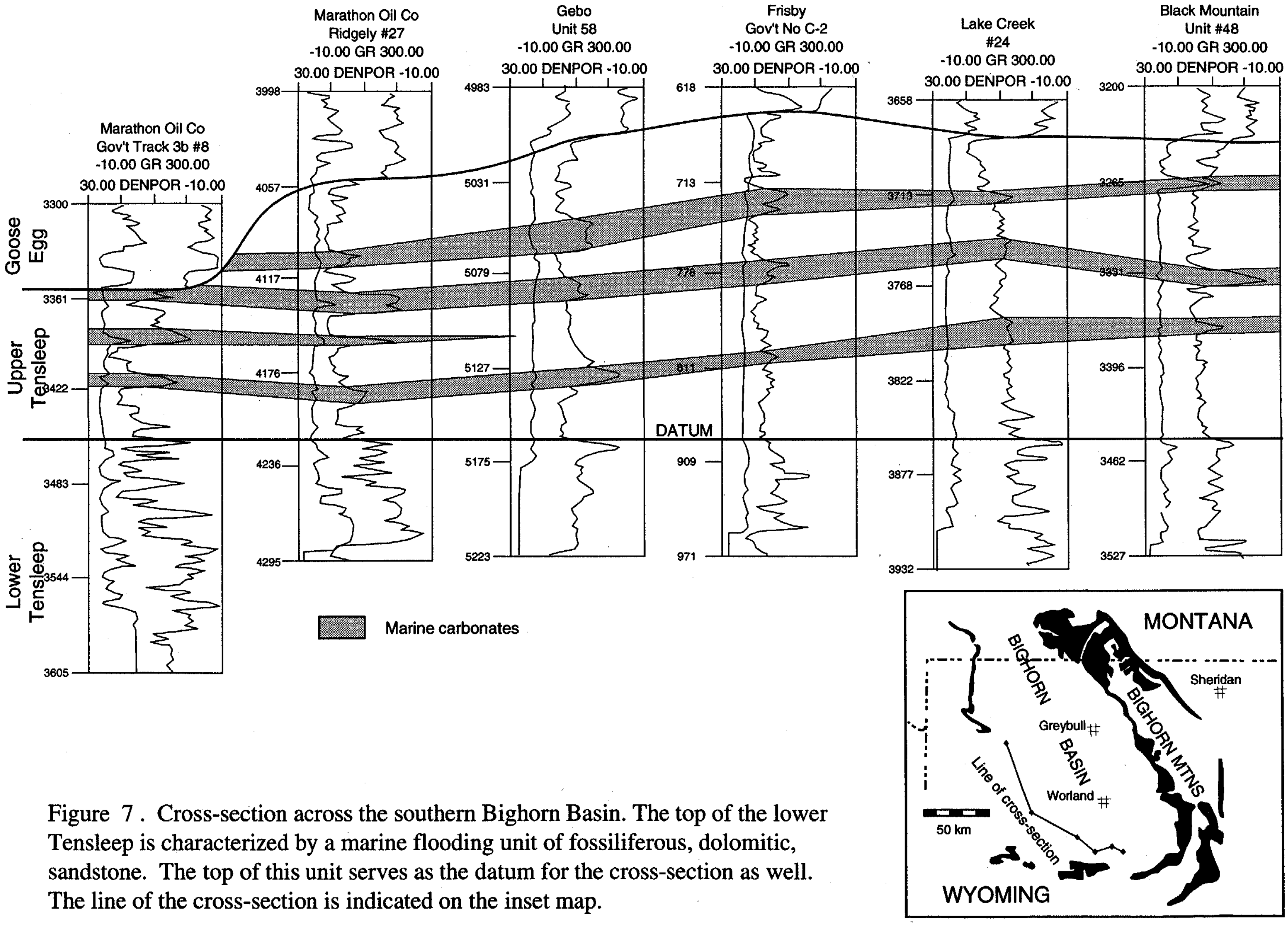

Figure 7 . Cross-section across the southern Bighorn Basin. The top of the lower Tensleep is characterized by a marine flooding unit of fossiliferous, dolomitic, sandstone. The top of this unit serves as the datum for the cross-section as well. The line of the cross-section is indicated on the inset map.

general it is more thinly bedded and less porous than the overlying upper Tensleep (Fig. 8). By contrast the upper Tensleep, ranges in thickness from 0 to 100 meters, is dominated by thick sets of eolian cross-strata punctuated by thinner fossiliferous dolomites. This study concentrates on the upper portion of the Tensleep because future incremental recovery from the Tensleep will come primarily from facies found in the upper unit.

Upper Tensleep cycles are composed of compound sets of eolian cross-strata gradationally overlain by sandy to fossiliferous dolomites capped by a sharp to erosional contact (Fig. 4). These cycles can be traced across the Bighorn Basin from the outcrop along the southeastern margin into the subsurface (Fig. 7). A single eolian unit may be composed of a single set of cross-strata or a series of sets, and individual sets vary in thickness from 1 to 17 meters. The sandy dolomitic units range in thickness from tens of centimeters to 8 meters.

Cross-stratified Units

The cross-stratified units of the upper Tensleep are not simple sets of cross-strata; rather they have extensive internal bounding surfaces. Kocurek (1988) described a hierarchy of bounding surfaces that occurs within eolian sequences based on their mode of origin (Fig. 9). Super bounding surfaces mark the cessation of eolian accumulation and as such are expected to be areally extensive (Fig. 9b). First-order surfaces mark the boundary created by the migration of climbing bedforms or draas. With the passing of simple dunes, a single set of cross-strata is produced. In the case of more complex bedforms or draas, the lee face may have superimposed bedforms which create second-order surfaces as they migrate down the lee face, thus creating a compound set of cross-strata (Fig. 9a). Finally, third-order or reactivation surfaces may occur within a set of cross-strata as a result of reorientation of the lee face under the influence of fluctuating flow conditions. Each of the surfaces will tend to contribute to the heterogeneity or compartmentalization of an eolian unit.

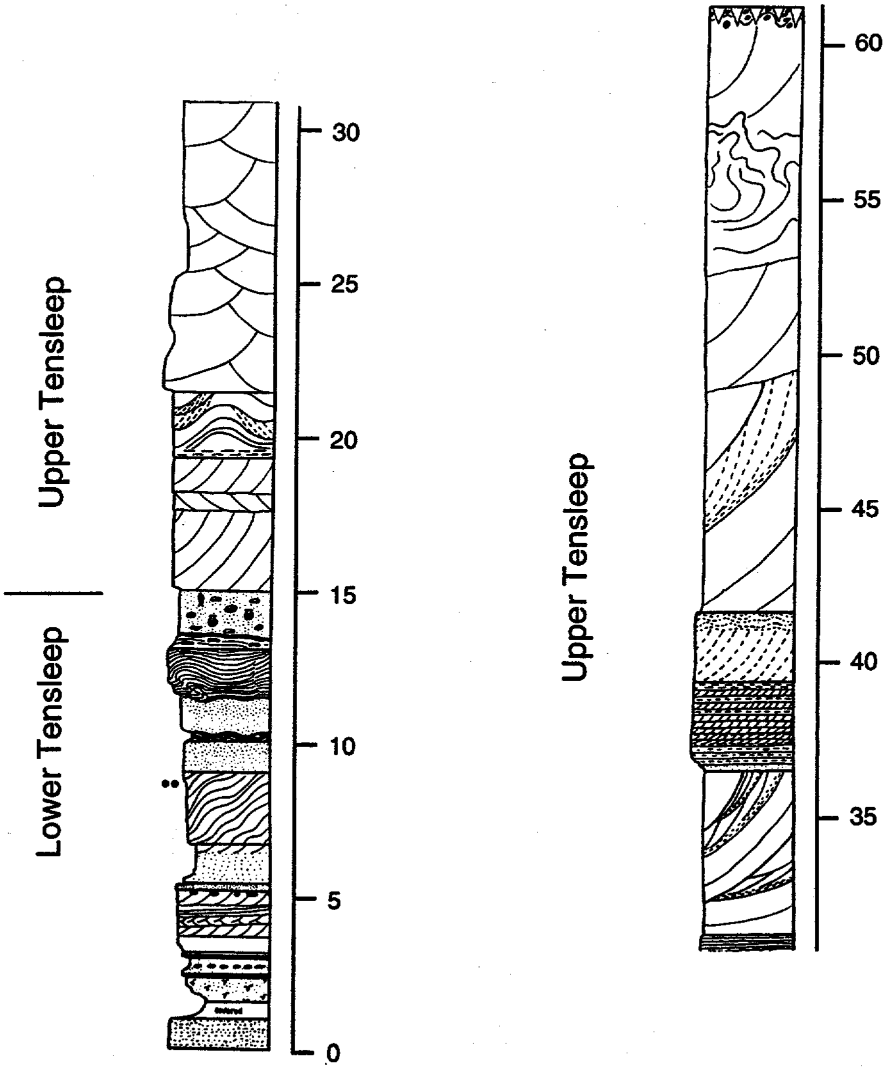

Figure 8. Vertical measured section from Ziesman Dome illustrating change from interbedded thin eolian sands and carbonates of the lower Tensleep to the thick sets of eolian cross-strata in the upper Tensleep. Black dots indicate samples Ah and Av taken from wind ripple laminated strata.

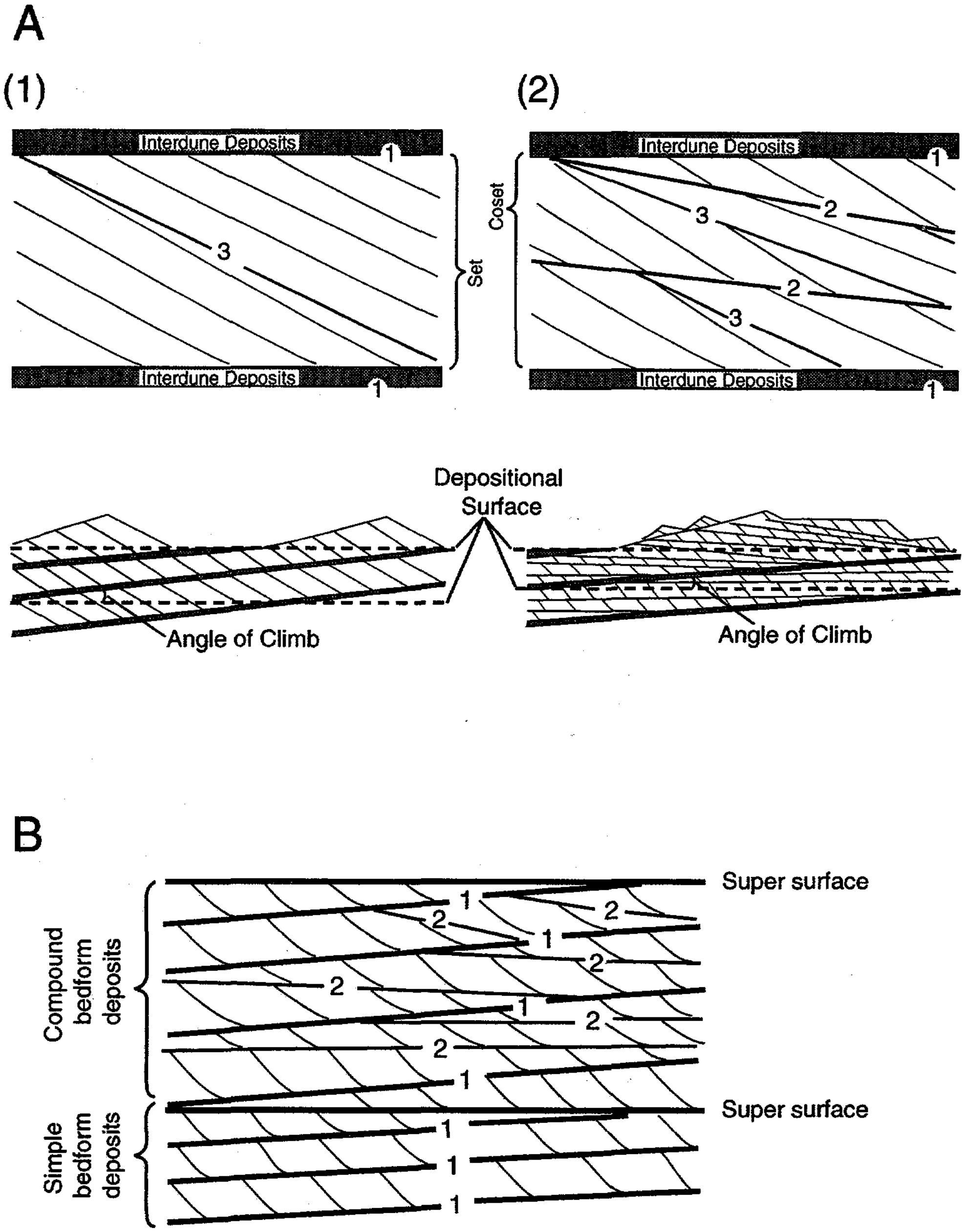

Figure 9. Figures showing hierarchy of bounding surfaces. (A) First-, second-, and third-order bounding surfaces are indicated by 1, 2, and 3. Angles of climb are measured with respect to the depositional surfaces. First-order surfaces formed by the migration of simple bedforms are illustrated in (1), and (2) illustrates how they form with the migration of compound bedforms. (B) Super bounding surfaces truncating first-order surfaces created by both simple and compound bedforms. From Kocurek, 1988.

Individual eolian units commonly are composed of a number of compound sets of cross-strata. At the Alkali Flats outcrops (Fig. 10), the extensive exposures made it possible to study the general character of the first-order surfaces that separate the accumulations of successive compound bedforms. The sets are separated by sharp, commonly gently undulatory surfaces. These first-order surfaces are at times associated with discontinuous lenses of flat to wavy-bedded, wind-ripple laminae. A single set of cross-strata can vary by several meters in its thickness along a single outcrop. Dip direction and magnitude was measured where possible on foresets and internal bounding surfaces and found to show a limited amount of variance from 175° to 285°, indicating a general transport direction to the southwest.

The cross-stratified sets are generally compound, but relatively simple sets also occur. However all of the sets show an internal cyclicity bounded by third-order or reactivation surfaces (Fig. 11). Figure 11b illustrates an observed and typical set of compound cross-strata. Sets of cross-strata are dominated by wind-ripple laminae with subordinate grain flow laminae. Foresets are systematically truncated by both the second- and third-order bounding surfaces to the SW. The cycles bounded by the third order surfaces are composed of low-angle wind-ripple laminae overlain by higher angle wind-ripple or grainflow laminae that are truncated by the next overlying third-order surface (Fig. 10). These cycles bounded by the third-order surfaces indicate cyclic changes in the orientation of the lee face as caused by systematic changes in flow conditions.

Sandy to Fossiliferous Dolomites

In the upper Tensleep the carbonate units are generally composed of a burrowed, dolomitic sandstone to dolomitized fossiliferous packstone. These units are laterally very continuous for tens of miles. The basal portions of these units can be intensely burrowed by Skolithos and Arenicolites (Wheeler, 1986). These grade upward into the more

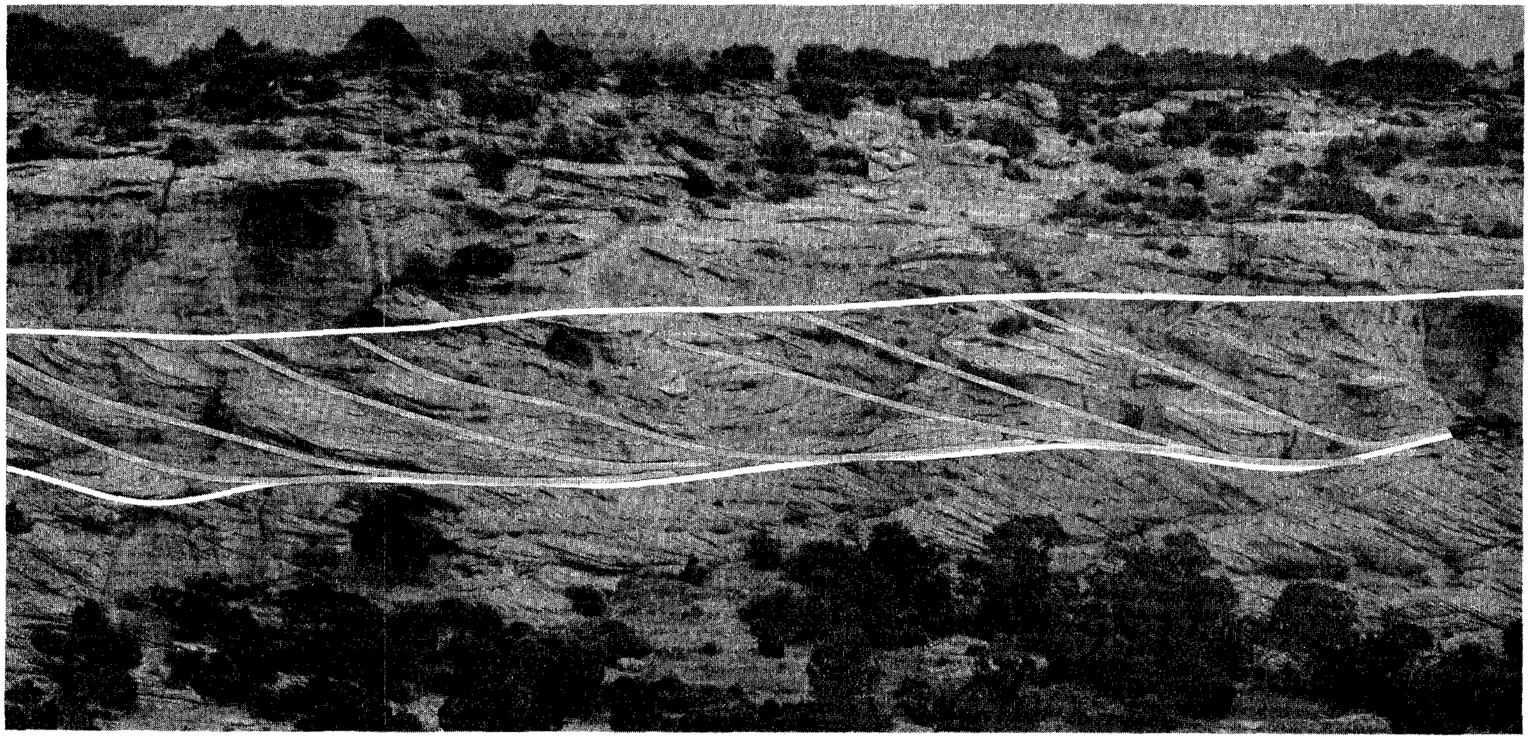

Figure 10. Photomosaic of a portion of the Alkali Flats outcrop, illustrating internal bounding surface geometries. The white lines indicate the first-order surfaces and the yellow lines are delineating the second-order surfaces. Note the undulatory nature of the first-order surfaces.

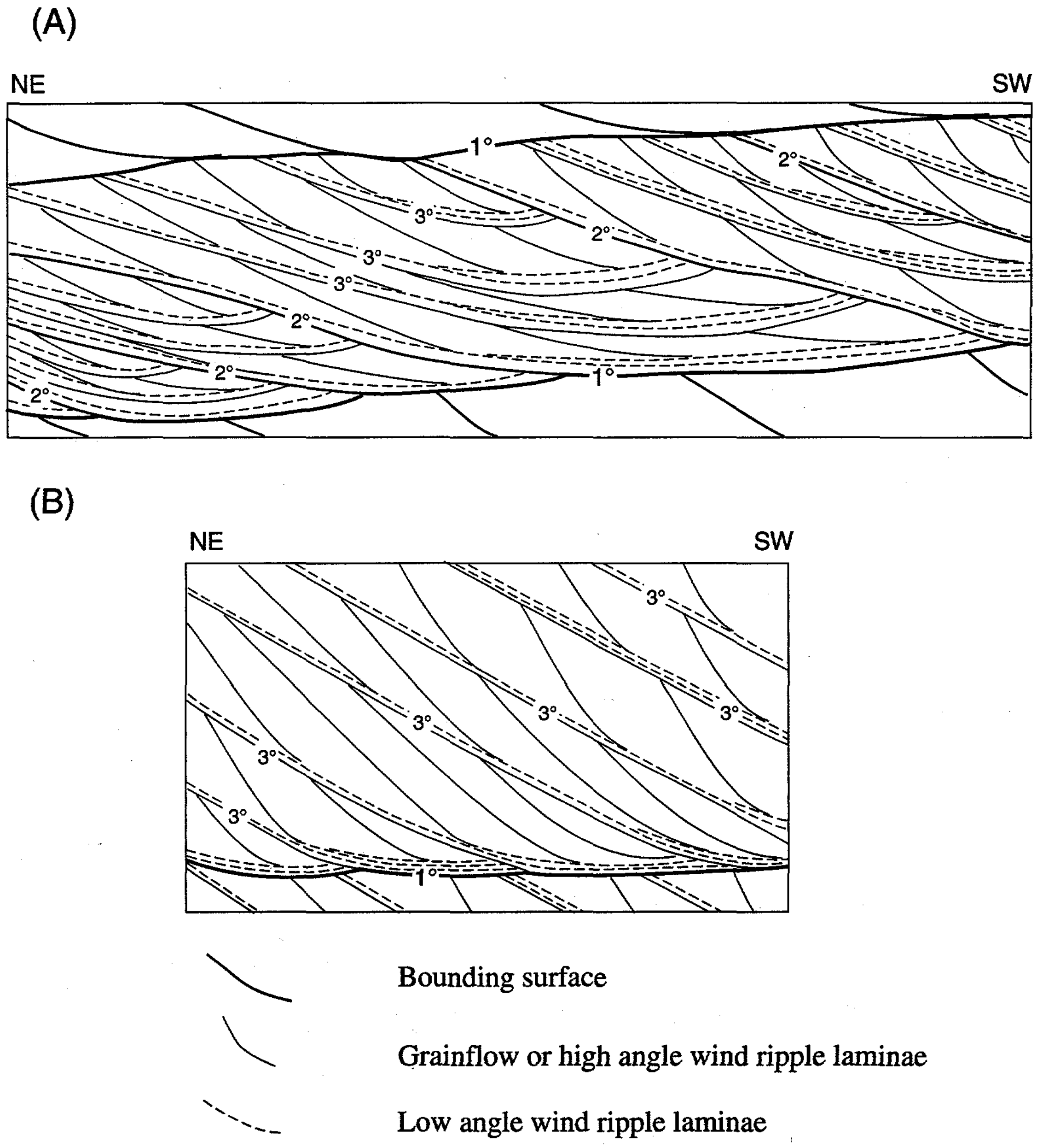

Figure 11. Detailed drawings of cross-strata, illustrating the internal bounding surface geometries typical of Tensleep cross-strata. First-order, second-order and third-order surfaces are represented by 1°, 2°, and 3° respectively. (A) Drawing of compound cross-strata at the Alkali Flats outcrop (Fig. 10). Cross-strata show two scales of internal cyclicity. The first is delineated by the 2° surfaces and is formed by superimposed bedforms. The second cyclicity is bounded by 3° surfaces and is formed by cyclic fluctuations in the leeface geometry. (B) Within the same eolian unit simpler cross-stratified sets occur that contain only cycles bounded by 3° surfaces.

fossiliferous dolomites that contain scattered corals as well as bivalves, gastropods, crinoid fragments, and fusulinids.

ENVIRONMENTAL INTERPRETATION

The upper Tensleep eolian-marine cycles represent accumulation during an overall regressive cycle punctuated by short-term transgressive events. During sea-level lowstands, large compound eolian bedforms migrated to the southwest across the exposed partially eroded carbonates of the previous cycle, under the influence of north-northeasterly winds (Fig. 6). In a manner similar to that described by Kocurek and Havholm (1993), flow deceleration within the upper Tensleep dry eolian system caused the migrating bedforms to leave thick accumulations of cross-strata. The area was subsequently flooded with the next relative rise in sea-level resulting in a cessation of eolian accumulation and the formation of a super bounding surface (Fig. 4). In this manner, the eolian accumulations were preserved by being placed below the regional baseline of erosion and capped by marine and marginal marine facies.

The interpretation of the Tensleep as a dry eolian system is indicated by the sharp planar nature of first-order surfaces that separate the sets of cross-strata, the paucity of interdune accumulations, and the lack of features within the accumulations suggesting a high water table. As described previously, the first-order surfaces at the Alkali Flats outcrop are undulatory and show several meters of relief. In a dry eolian system where the depth of scour within the interdune areas is controlled strictly by aerodynamic factors and is not limited by a water table or other barrier, the depth of scour is expected to vary from place to place and through time as a function of dune spacing and variations in the local wind velocity (Paola and Borgman, 1991; Crabaugh, 1994). This same variation in scour depth might allow some of the most deeply scoured interdune areas to intersect a local water table or be an area for water accumulation, thus forming the discontinuous lensoid shaped interdune accumulations of flat- to wavy-bedded strata characteristic of the Alkali Flats area.

To reconstruct the bedforms which produced these accumulations, the orientation of internal bounding surfaces and cross-strata were measured using a Brunton compass. Where the sets were compound and result from the migration of superimposed dunes over a larger bedform, the stereonet method of Rubin and Hunter (1983) was used to reconstruct the configuration of the superimposed and main bedforms. Averaging the results indicates the main bedforms were moving to the southwest at approximately 205°, while the superimposed bedforms were moving to the west at approximately 291°. Utilizing all the available outcrop data the bedforms have been simulated using Rubin (1987) computer modeling program (Fig. 12).

The cross-strata cycles bounded by the third order surfaces and composed of low-angle, wind-ripple laminae overlain by higher angle, wind-ripple or grainflow are interpreted to represent periodic fluctuations in the wind regime. The lower-angle, wind ripple laminae represent times of more oblique flow when the lee face is experiencing more along-slope transport. The higher angle, wind-ripple laminae and grainflow probably correspond to times of more transverse airflow over the dunes when a slip-face was developed. These cycles are interpreted to represent annual fluctuations in the wind directions, and therefore they would also correspond to the annual forward migration of the bedforms. The annual fluctuations in wind direction postulated by the climatic models of Parrish and Peterson (1988) are consistent with these interpretations (Fig. 6).

EFFECTS ON RESERVOIR HETEROGENEITY

For the first time this study considers eolian reservoir heterogeneity as a function of the controls on accumulation and preservation of eolian sediments. The most apparent reservoir heterogeneity is the vertical compartmentalization of the Tensleep by the marine carbonates, which tend to be more heavily cemented than the intervening sandstones.

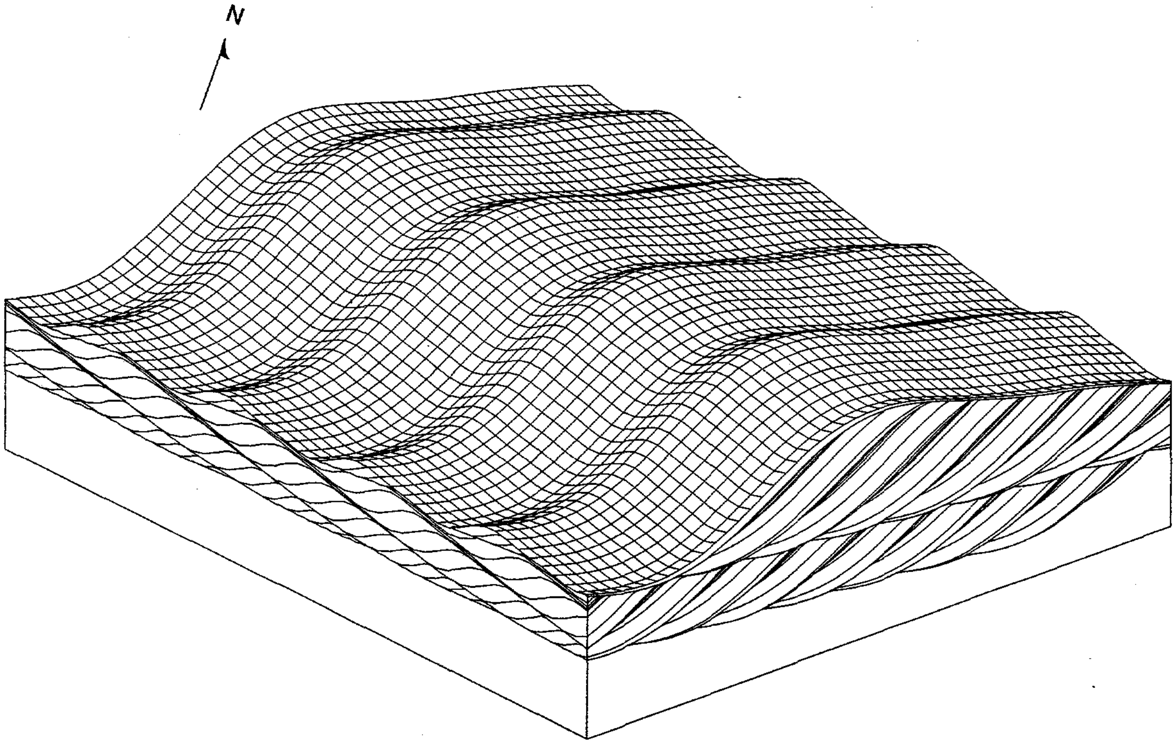

Figure 12. Generalized Tensleep Sandstone compound bedform as reconstructed using Rubin, 1987. The main bedform is migrating to the southwest at approximately 205° and the superimpsed bedforms are migrating to the west at approximately 291°.

These units can be traced over great distances as illustrated in Figure 7. This large-scale heterogeneity is controlled by basin-scale changes in relative sea-level that control the ultimate preservation of the reservoir rocks.

Smaller-scale heterogeneities are related to the style of accumulation within the Tensleep eolian system. Flow within the Tensleep cross-stratified units is expected to be heavily effected by the hierarchy of bounding surfaces as well as spatial variation in stratification type. For example, the low-angle wind-ripple laminae which form the basal portion of the cycles that are bounded by third-order surfaces, are expected to be more tightly packed and therefore more heavily cemented than the thicker wind-ripple and grainflow laminae which overlie them. This small-scale heterogeneity occurs throughout the Tensleep in both surface and subsurface samples.

FUTURE PLANS

The primary goal for Task 1.0 in the coming year is the integration of outcrop and subsurface data into regional lithofacies correlations. This work forms the heart of the effort to place the results of Task 2.0, that is the relative permeability anisotropy, into a regional and process-based context. During this winter efforts will concentrate on the subsurface aspects of the study. Description and interpretation of core will continue for both the Bighorn and Wind River basins. Using the software Production Analyst©, this data is being integrated with the existing database of digitized well logs and core analyses. Production Analyst allows us to interactively construct maps and cross-sections and easily divide the Tensleep into correlatable lithofacies packages (Fig. 7).

Field studies will continue in the summer of 1995 in the northern Bighorn Basin and around the margins of the Wind River Basin. The primary objectives of the fieldwork will be to determine the extent of interbasin correlation of units within the Tensleep and to determine to what extent different Tensleep eolian units are distinct from one another with respect to internal fabric. The photo-documentation of relevant reservoir and bounding surface lithologic character and dimensions will be concluded in the second year.

A principal objective for sampling during the second field season will be to collect representative samples across and along representative bounding surfaces. These samples will be used in the coreflood experiments of Task 3.0 and the relative permeability and image analysis investigations in Task 2.0.

The petrologic studies of Task 1.0 will focus on building a database of diagenetic modeling and cement distributions necessary for the construction of a regional diagenetic framework.

TASK 2.0 - RELATIVE PERMEABILITY MEASUREMENTS.

OBJECTIVES

The focus of this task is to obtain quantitative laboratory data on the magnitude and variability of relative permeability anisotropy and spatial variation of the dominant reservoir and boundary surface lithologies of the Tensleep Sandstone. Existing data will be collected, compiled, and placed within the regional frameworks constructed in Task 1.0. Relative permeability will be measured at UW using the unsteady-state technique. An additional objective of this study is to provide algorithms for calculating relative permeability from quantitative pore imagery data.

INTRODUCTION

The construction, testing, and calibration of the apparatus has been completed. We have established procedures to be used to measure relative permeability. The laboratory work for measurement of relative permeability is ahead of schedule. We have obtained Tensleep wind ripple laminated eolian sandstone from the Owl Creek uplift, the structure that separates the Bighorn and Wind River basins. We have also obtained crude oil form the Black Mountain oil field (Texaco). This crude oil has typical Tensleep viscosity and °API gravity. The oil will be the principle hydrocarbon used for the experiments. In the laboratory, we have cut cores both parallel and perpendicular to bedding planes and have commenced permeability analysis. The plugs have been flooded with both water and oil. Apparatus pressures are high due to relatively low permeability and high oil viscosity (100cps).

A field coring device (a modified chain saw) has been successfully fitted to cut the required 1.5 inch cores. Cores from very porous grainflow laminated Tensleep (a laminae typical of the upper Tensleep) have been difficult to obtain using the portable drill. A drill press was purchased and setup in order to drill these samples in the lab using either air or liquid nitrogen.

The following is a detailed discussion of the techniques used in the relative permeability measurement and data analysis. Each core is sized, dried, measured, evacuated, and weighed. Porosity and permeability to air are determined initially, then the core is saturated with water. The saturation process takes several days, and is culminated by measurement of permeability to 100% water saturation. Oil is then forced into the core until a saturation of approximately 25% water is obtained prior to beginning the two-phase flow experiments. Finally, the oil is displaced by water at constant injection rate for an unsteady-state relative permeability measurement.

This complete process has been achieved on four cores (Table 3), while most are still at intermediate stages. We present complete results from two core plugs from a Tensleep sandstone sample from Ziesman Dome, Wyoming (see Figure 8 for geologic setting). One core is vertical (Av) that is perpendicular to stratificatin; the other is horzontal (Ah) and parallel to bedding

Oriented samples are obtained as close together as practically possible in an attempt to measure flow properties at the same location. Of course this is not possible since core holes must be separated physically by at least a centimeter to operate the coring device. In spite of these small separations, the sample pairs appear to be very similar to each other. Cores oriented horizontally are probably most similar to flow laterally from well to well, while the vertical samples measure cross-flow between layers and across laminations and bounding surfaces These considerations will be addressed in future reports.

CORE MEASUREMENTS (DRY)

We begin with basic measurements of the core dimensions:

Sample Av:	length 6.54 cm	diameter 3.69 cm	weight 160.836 gm
Sample Ah:	length 5.23 cm	diameter 3.71 cm	weight 125.153 gm

Table 3. Relative permeability sample status.

A total of 48 cores have been assembled for this project:
5 cores were used for initial testing (Casper and Berea sandstones)
14 cores from the subsurface have not been used yet.
9 cores are measured and being dried.
6 cores have had only air permeability measured.
2 cores have brine saturation and await oil flood.
12 cores have been flooded with both oil and water (completed).

Core	porosity	air perm	brine perm	oil perm	kro/krw
1v	.2175	.65 md	too low for apparatus		
2v	.2250	427.7	127	240	yes
3v	.2348	423.3	190	183	yes
4h	.1223	155.8	122	103	yes
5h	.223	461.3	361	196	yes
6h	.239	618.6	504	264	yes
7h	.235	470.8	368	192	yes
8h	.228	469.5	405	182	yes
Ah	.158	161.7	114	88	yes
Av	.137	104.9	89	56	yes
Bv	.154	14.1	7	3	yes
Bh	.171	78.4	51	38	yes
Cv	.172	158	136		
Ch	.167	138	108		
Dv	-	101			
Dh2	-	162			
Dh3	-	244			
Ev	-	547			
Eh1	-	344			
Eh2	-	443			
Gh1	now being dried				
Gh2	"				
Gv	"				
Hv	"				
Hh1	"				
Hh2	"				
Iv	"				
Ih1	"				
Ih2	"				

We then flow nitrogen though each core at ambient conditions to obtain air permeability. A differential pressure of 0.6122 atm was maintained across each core, and the following measurements were observed using a Ruska permeameter:

Sample Av:	$Q_g = 8.370$ cc/sec	$k_g = 104.87$ md
Sample Ah:	$Q_g = 16.33$ cc/sec	$k_g = 161.67$ md

These computations are made by assuming Darcy's law, the physical dimensions listed above, and using additional physical properties appropriate for the altitude at Laramie, Wyoming:

Air viscosity = 0.0178 cp and Downstream pressure = 0.7733 atm.

Note the appropriate correction for Laramie, Wyoming ambient atmospheric pressure (11.4 psia at 7200 ft elevation) is included, but no corrections for Klinkenburg effect are made. Since low pressures and low flow rates are used, and the air permeability measurements are not crucial at present, the accuracy of these measurements is considered adequate.

The gas permeabilities of the two samples are similar (105 and 162 md), confirming the accurate sampling of similar spots in the sandstone. The vertical permeability is slightly lower, as expected in a laminated sample where flow is across layers are constrained by change in pore structure. Horizontal permeability flows parallel to layering and is commonly higher. Of the ten sample pairs examined to date (twenty cores), 7 of 10 show this absolute permeability anisotropy (Fig. 13).

CORE MEASUREMENTS (WET)

The next step is to saturate each core with a brine solution by soaking the samples in brine for one week. This step is also necessary prior to flowing water through the core. The wet weight can then be compared to the dry weight to estimate sandstone porosity.

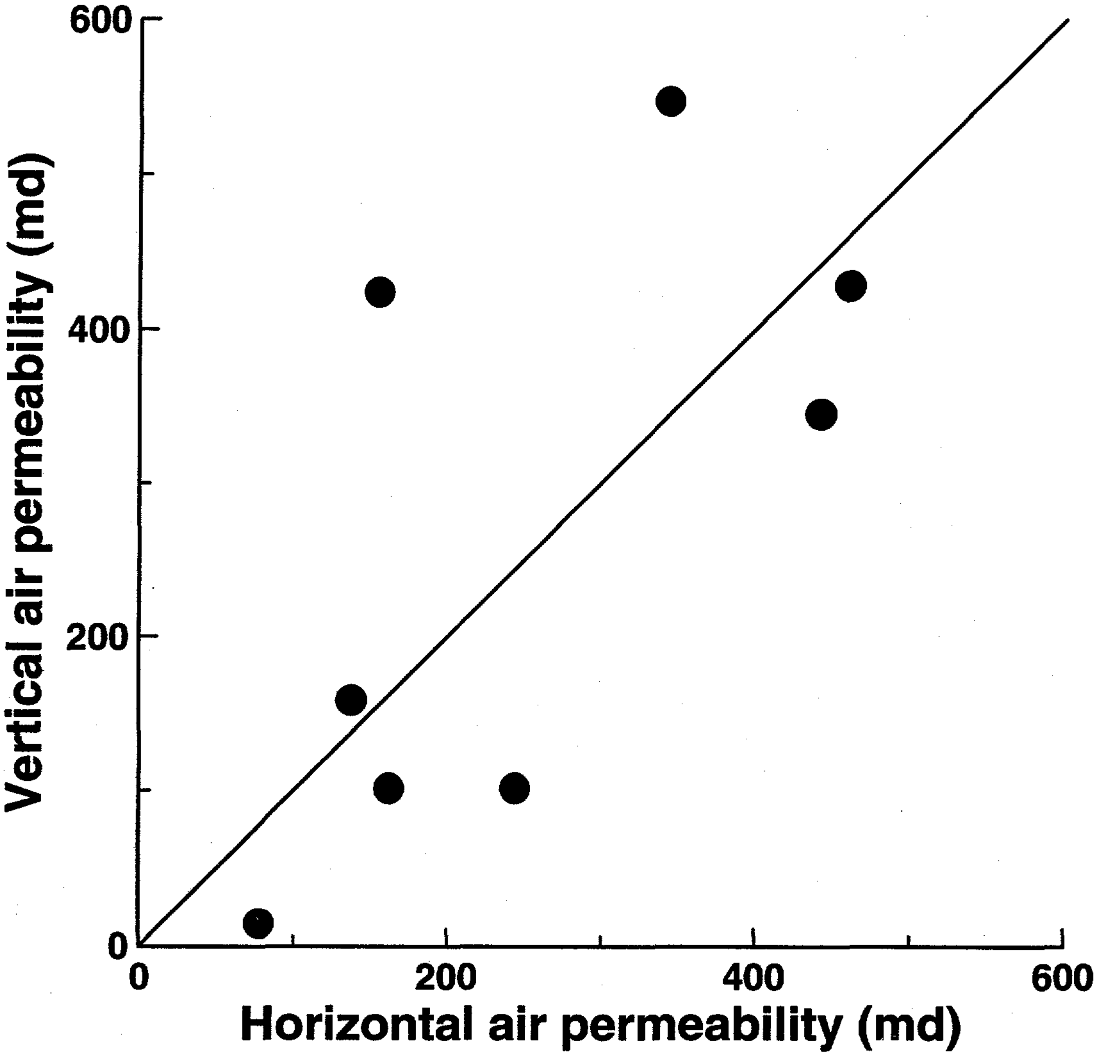

Figure 13. Tensleep sandstone samples, vertical versus horizontal air permeabilities.

Such a calculation will possibly yield a slightly low porosity, as all pore spaces might not yet be saturated. The brine used is KCl with a density of 1.009 gm/cc.

Sample Av:	wet weight 170.49 grams,	pore volume = 9.57 cc	ϕ = 13.7%
Sample Ah:	wet weight 134.20 grams,	pore volume = 8.97 cc	ϕ = 15.8%

Of these data, only the pore volume (V_p) is crucial for subsequent relative permeability calculations.

Absolute permeability to water is established by flowing KCl water through the core which is now 100% water saturated. Ideally, the absolute permeability to 100% water should be identical to the air permeability determined with the Ruska permeameter. This is seldom the case. In an attempt to correct for the difference between the gas versus water absolute permeabilities, water is flowed through the cores at different rates until a water permeability is obtained very near the air permeability. For example, on the Ah and Av cores, the following data were obtained:

Core	dP (psi)	Qw (ml/hr)	kw (md)	
Ah	0.23	40	329	
Ah	1.18	100	162	Ah air perm = 162 md
Ah	1.97	200	194	
Av	0.86	40	113	Av air perm = 105 md
Av	2.73	100	88.5	

where Qw = flow rate of water through core
dP = pressure differential from inlet to outlet, and
kw = calculated permeability from Darcy's law.

The permeability closest to the air permeability is selected for the relative permeability calculations, although any (dP, kw) pair could be used for normalization of the relative permeability plots to a scale of zero to one.

Finally, the water saturated core is flooded with oil. We attempt to reduce the water saturation to a constant 25% in each core, so that the comparison of relative permeability curves will be from a common initial water saturation base. The 25% water saturation is achieved by calculating how much water must be removed from the core to achieve this saturation, and flowing sufficient oil until that much water is recovered. When the desired saturation is achieved, the ambient pressure drop and flow rate then yield another reference point, the effective permeability to oil at initial water saturation (ko@Swi). The following data were obtained:

Core	Oil injected	Water produced	dP	Qo	Swi	ko@Swi
Ah	37.3 cc	6.75 cc	9.21 psi	45 ml/hr	.247	87.9 md
Av	73.5 cc	7.68 cc	9.01 psi	22 ml/hr	.247	55.8 md

The pressure drop across core Av is slightly higher, but the core is slightly longer and the injection rate lower, so Darcy's law actually yields a lower permeability. The relative permeability experiments can now begin, because the preliminary measurements have been made on the partially saturated cores.

FRACTIONAL FLOW

Relative permeability is derived from fractional flow curves, essentially as outlined by Willhite (1986) in the SPE Textbook on Waterflooding. A constant injection rate of water is maintained in what is commonly known as an "unsteady-state" experiment because the water saturations vary constantly throughout the core and with time. Since we measure outflow at the outflow end, the measurements should be interpreted as flow conditions at the outflow end. Buckley-Leverett theory is used to derive flow properties as follows:

Define the following variables:

$\overline{S_w}$ = average water saturation throughout core,
S_{w2} = saturation at outlet end of core,
Q_i = pore volumes of water injected,
f_{w2} = fractional flow of water measured at outlet end, and
f_{o2} = fractional flow of oil measured at outlet end.

From Buckley-Leverett theory, a fraction flow curve plotted against water saturation can be used to predict waterflooding performance. At any point past breakthrough of the water, the slope of f_w versus S_w is inversely proportional to the pore volumes of water injected. This can be written mathematically as:

$$(1/Q_i) = (df_w / dS_w) .$$

If such a slope is drawn graphically, then the top end will be at S_w and f_w=1.0, while the tangent touching the fractional flow curve is at S_{w2} and f_w=f_{w2}. By definition of f_w we can also use the fact that f_{w2}=1-f_{o2} and derive the following equation:

$$(d f_w / d S_w) = (1 - fw2) / (\overline{S_w} - Sw2) = fo2 / (\overline{S_w} - Sw2) .$$

Combining the two equations above, we can derive the simple linear formula:

$$\overline{S_w} = Q_i \, fo2 + Sw2 ,$$

Which means that a plot of average water saturation versus pore volumes water injected, will be a straight line with intercept at S_{w2} the saturation of the outlet core end. Figure 14 demonstrates the procedure as outlined by Willhite (1986). Fractional flow of water (f_w) is determined from the produced water and oil volumes collected at the outlet end:

$$f_w = 1 - f_o.$$

Once the saturations S_{w2} are found, another plot of f_{w2} versus S_{w2} can be easily prepared. For Tensleep samples Av and Ah, such plots are displayed in Figures 15 and 16. In these figures the vertical core exhibits nearly "piston" displacement, where the output goes instantly from all oil (f_w=0) to nearly all water (f_w=1) when water breakthrough occurs. The horizontal core exhibits more of a classic fractional flow behavior, showing a gradual increase in f_w with increasing water saturation.

These data can now be used to calculate relative permeability by first solving for apparent viscosity of the two-phase system, and again using a graphical intercept technique as described by Willhite (1986). The apparent viscosity is found from:

$$\overline{\lambda^{-1}} = (q_b \mu_b \Delta p) / (q_t \Delta p_b)$$

where the b subscript denotes quantities (flow rate, viscosity, and pressure difference, respectively) taken from the base single-phase conditions, and the other parameters are from the oil-water flowing experiment. Total flow rate q_t is constant at 40 ml/hr from the water pump, and the variation of pressure with time is noted during the experiment. Apparent viscosity is then plotted against pore volumes injected, and the intercept yields apparent viscosity at the outflow end. The procedure is derived by Willhite (1986) and shown here in figure 17 from his examples.

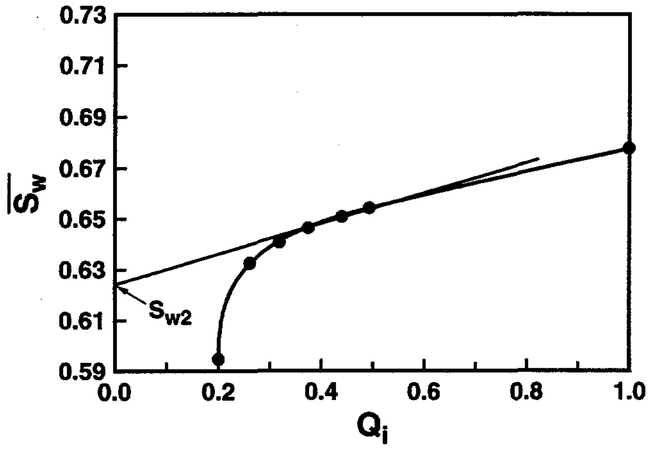

"Figure 3.28–Expanded plot of $\overline{S_w}$ vs. Q_i to obtain slopes for computation of S_{w2} and relative permeability ratios." From Willhite, 1986.

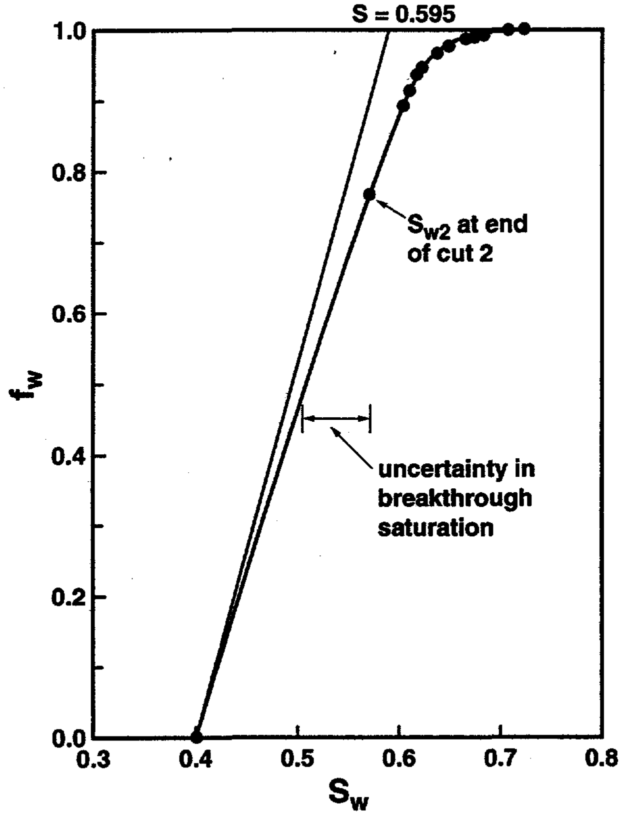

"Figure 3.29–Fractional flow curve obtained from experimental data." From Willhite, 1986.

Figure 14. Examples from Willhite (1986) for determining outlet end water saturation and the associated fractional flow curve from laboratory displacement data. This Figure 3.28 is equivalent to our Figure 15, and this Figure 3.29 is equivalent to our Figure 16 for our Tensleep laboratory data.

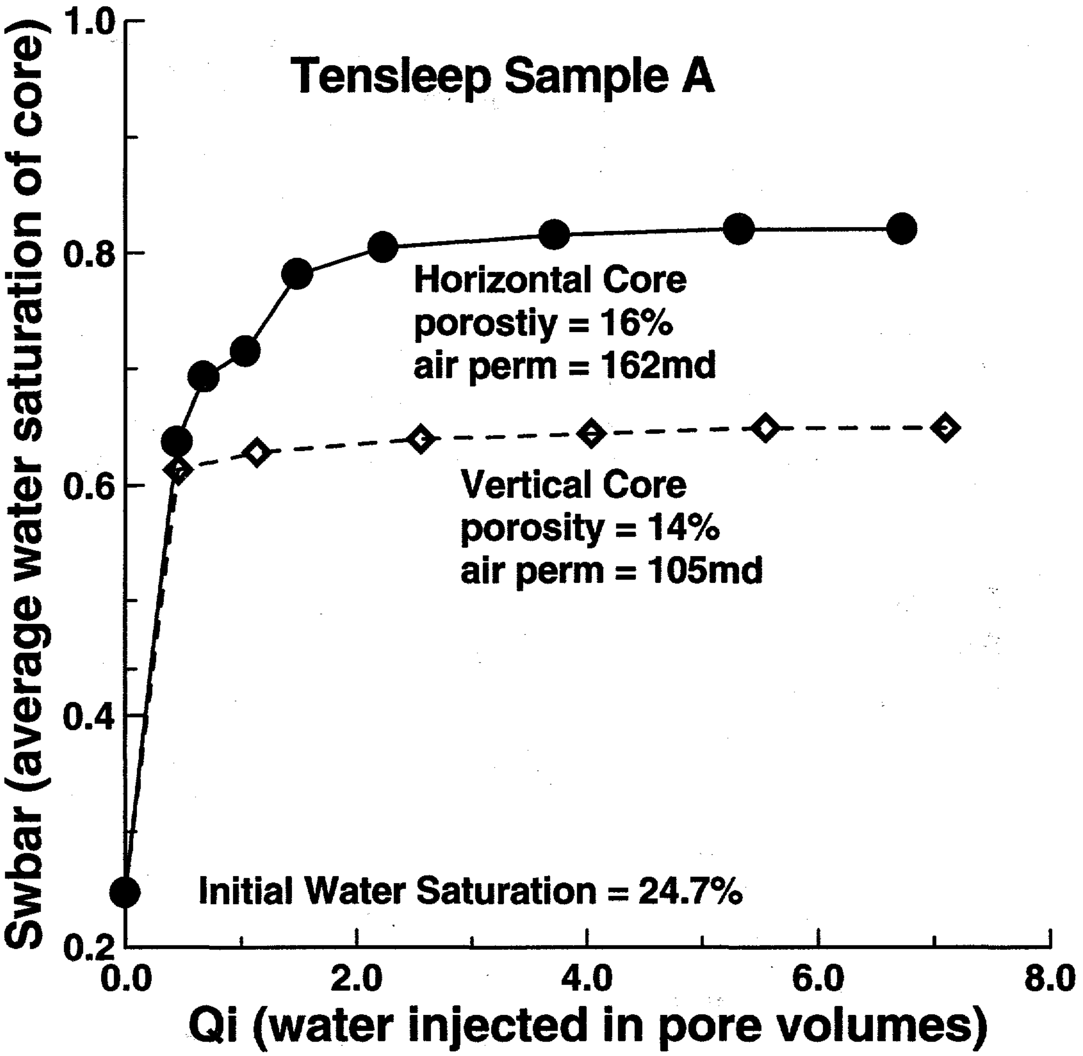

Figure 15. Average core water saturation versus pore volumes of water injected, similar to example 3.28 shown in Figure 14.

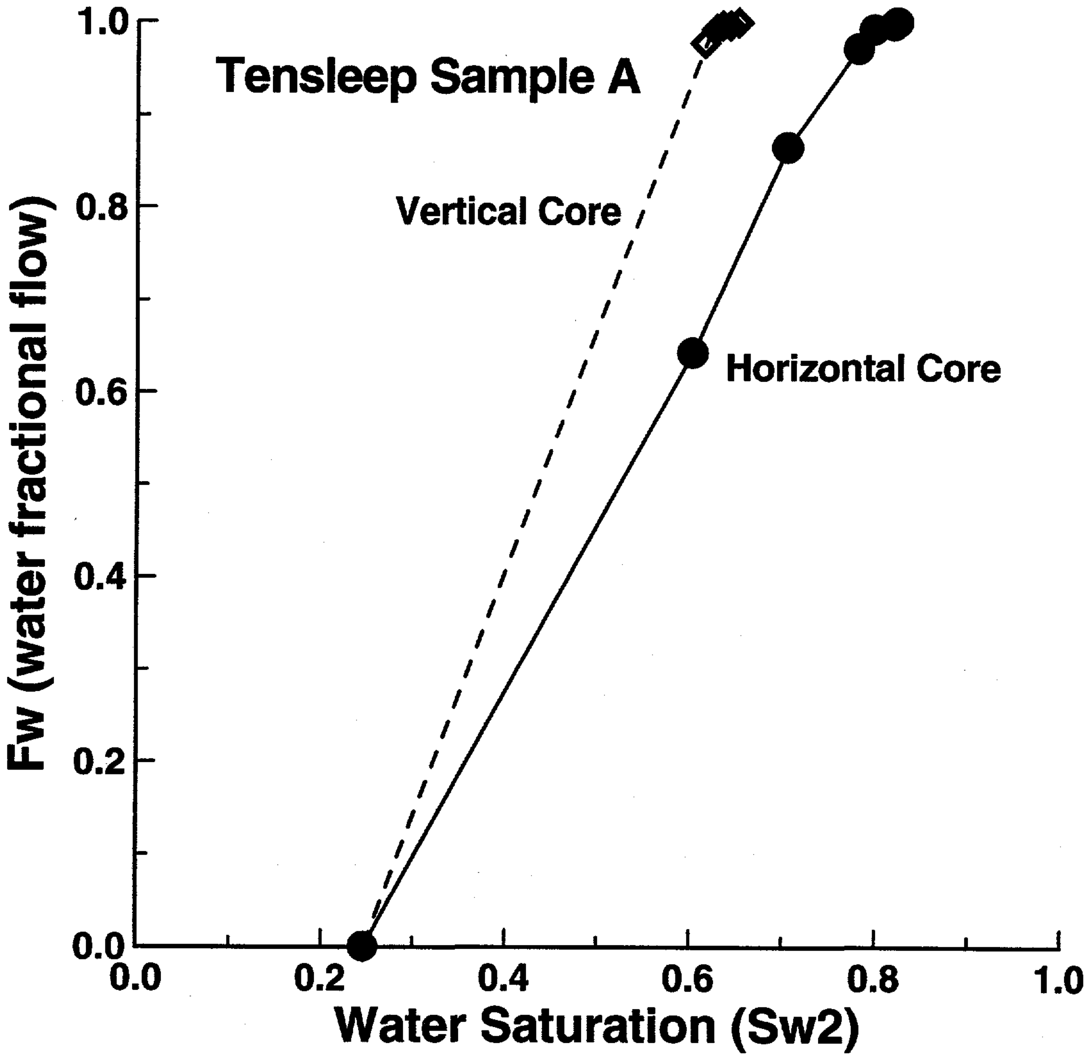

Figure 16. Fractional flow versus outlet water saturation, similar to example 3.29 shown in Figure 14.

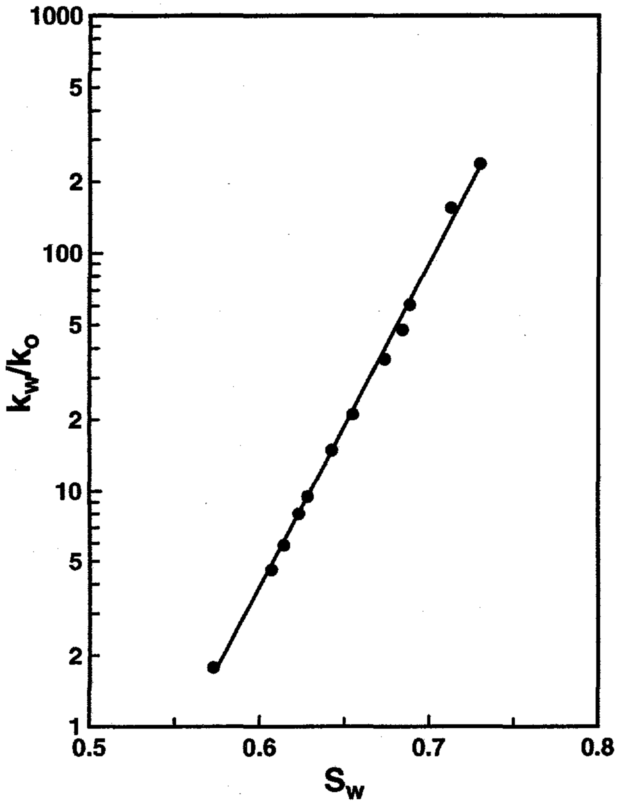

"Figure 3.30–Computed relative permeability ratio vs. water saturation." From Willhite, 1986.

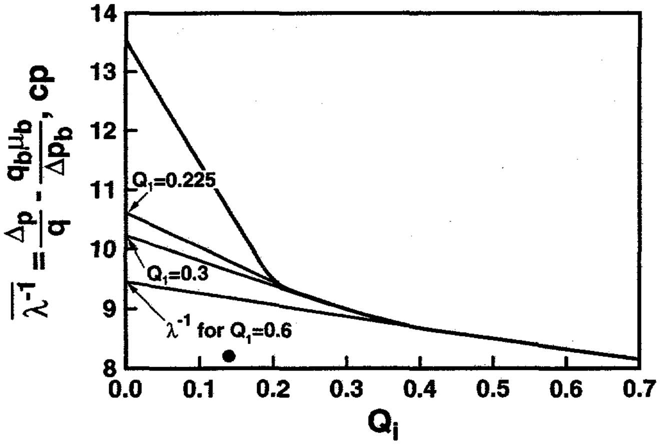

"Figure 3.31–Construction for determining outlet-end effective viscosity from average values." From Willhite, 1986.

Figure 17. Examples from Willhite (1986) showing the technique for finding apparent viscosity from displacement data. This Figure 3.30 is equivalent to our Figure 19, and this Figure 3.31 is equivalent to our Figure 18.

For Tensleep samples Ah and Av the following laboratory data were obtained:

	time (min)	pressure (psi)	liquids (cc)	oil (cc)
Sample Ah:	6	10.8	3.5	3.5
	9	9.7	5.9	4.0
	14	8.5	9.8	4.2
	20	7.9	14.2	4.8
	30	7.6	21.3	5.0
	50	7.5	34.8	5.1
	72	7.5	49.5	5.15
	91	7.5	62.3	5.15
Sample Av:	6	25.2	3.5	3.5
	16	24.6	10.3	3.65
	37	24.5	24.2	3.75
	58	24.4	38.5	3.80
	80	24.3	53.3	3.85
	102	24.2	68.6	3.85

Experiments are performed until no additional oil is displaced from the core. The two samples reached water breakthrough at about the same time (6 minutes) and with the same cumulative oil produced to that time, but sample Av yielded very little additional oil past that time. This indicates that the absolute permeabilities and volumes are very similar when vertical and horizontal cores are compared, yet the characteristics of flow are quite different.

From the above data table, the following calculations are made:

	Qi	$\overline{S_w}$	fo	apparent viscosity
Sample Ah:	0	.247	1	
	.45	.637	1	
	.68	.693	.357	25.9 cp
	1.04	.715	.052	22.7
	1.49	.782	.135	19.2
	2.23	.805	.028	16.9
	3.72	.816	.0074	16.2
	5.32	.821	.0034	16.1
	6.73	.821	0	15.9
Sample Av:	0	.247	1	
	.46	.613	1	
	1.14	.628	.022	29.36
	2.56	.639	.0072	28.9
	4.40	.644	.0035	28.86
	5.55	.649	.0034	28.84
	7.1	.649	0	28.82

These data were used to prepare Figures 15 and 16. Note for sample Ah the odd data point at Qi=1.04 where the fractional flow of oil decreases unreasonably. In Figure 15 this appears as a deviation from the increasing curve. The reason for such behavior is probably due to a few drops of oil leaving the core early (or late) due to capillary pressure end effects. It would be reasonable to smooth the data by distributing the produced oil equally across adjoining time increments, but instead we edit the one point out, and it is not used in subsequent plots. Overall, the results are still the same when comparing vertical with horizontal, and we can verify that all points are actual measurements with no data smoothing.

Figure 15 is used intensely to draw tangents and calculate the outlet end saturations S_{w2}. The results of drawing tangents at each data point are summarized in the next table of data. First, we plot apparent viscosity versus outlet water saturation, and draw similar tangents as described by Willhite (1986). This plot is shown in Figure 18.

Once the working plots (Figs. 15 and 18) are enlarged and tangents drawn at each data point, the intercepts can be read and assembled into another table of interpreted data. This table then becomes the first interpretive set of data, as the previous sets of numbers are all calculated by straight forward equations relating the various measured quantities. The intercepts from the plots yield the following results:

Let S_{w2} be the intercept from tangent lines in Figure 15, and let v_2 be the apparent viscosity intercepts read from tangents drawn on Figure 18.

	Sw2	v2
Sample Av:	.247	
	.614	29.36
	.626	28.9
	.633	28.86
	.641	28.84
	.65	28.82
Sample Ah:	.247	
	.603	25.9
		22.7
	.704	19.2
	.78	16.9
	.797	16.2
	.818	16.1
	.822	15.9

As derived by Willhite (1986) the ratio of relative permeabilities can then be derived simply by calculating:

$$k_{rw}/k_{ro} = (\mu_w f_w 2/\mu_o f_o 2)$$

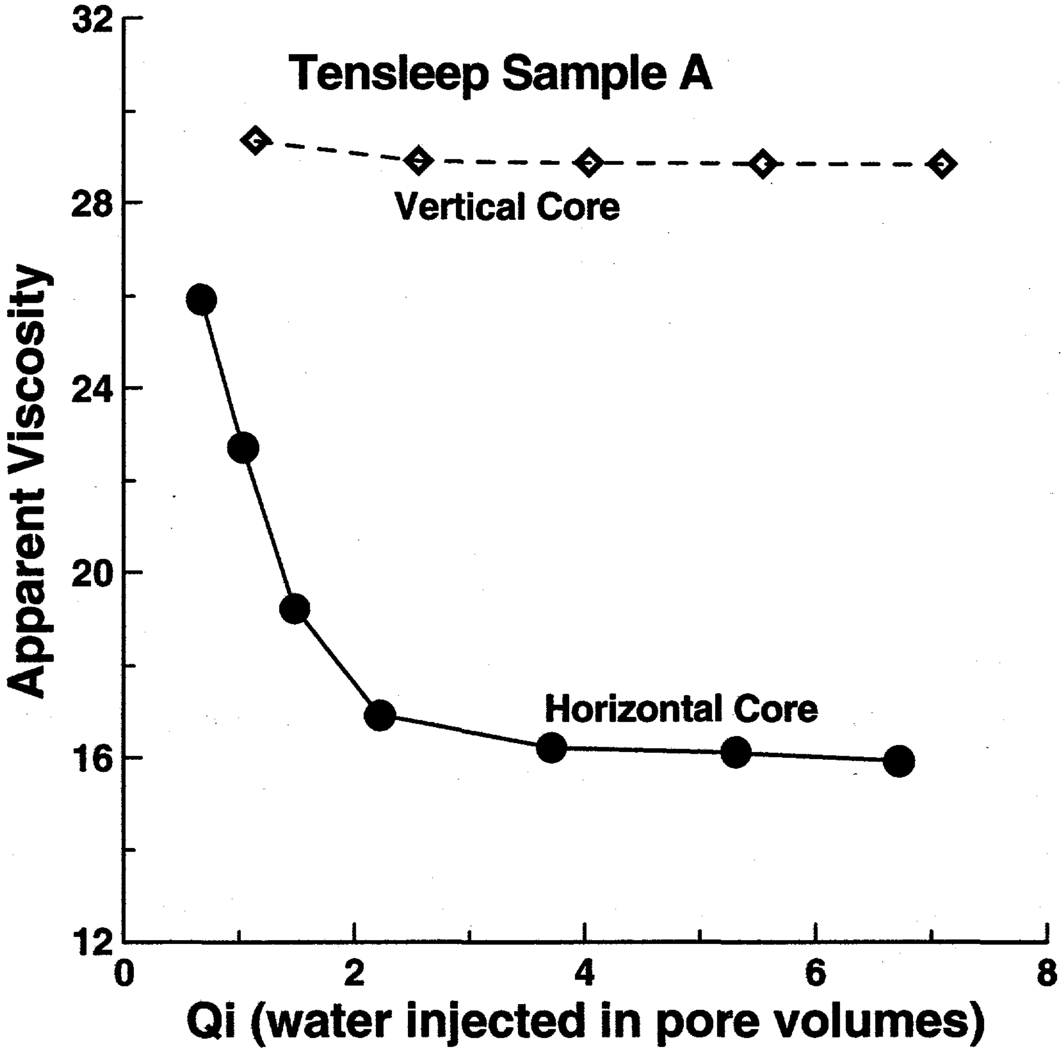

Figure 18. Apparent viscosity versus pore volumes water injected to determine relative permeability of oil and water. Similar to example 3.31 shown in Figure 17.

This is shown for samples Av and Ah in Figure 19. Ideally, these points should be on a straight line, similar to the results shown previously in Figure 17. We are in the process of determining how a better line can be obtained, and whether smoothing techniques can be justified for these data.

SUMMARY

Relative permeability measurements have been completed on a few cores, and the procedures used are being reviewed to determine if further modifications might be justified. Our results do not yield curves as smooth as we had hoped, but this is the norm when working with actual heterogenous rock samples. We will improve the procedures by more accurately measuring the quantity of displaced oil as a function of time, and obtaining more data points during the time interval between water breakthrough and final displacement of oil.

FUTURE PLANS

The primary goal of Task 2.0 will be the measurement of relative permeability for tens of samples and the calculation of relative permeability anisotropy. Pore image data collection and analysis will proceed in the second year. The Task 2.0 effort will include studies of gas permeability heterogeneity in vertical profiles.

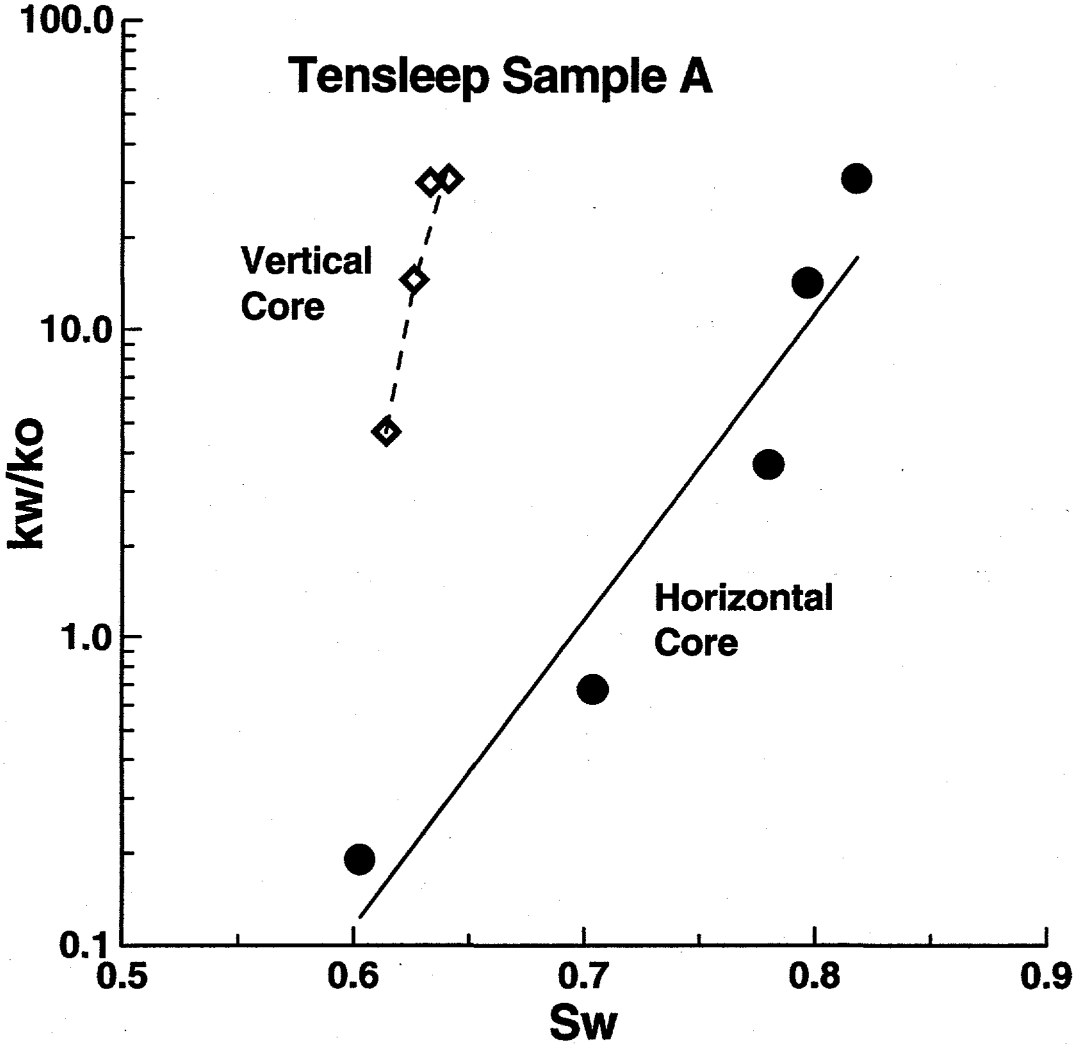

Figure 19. Relative permeability ratio versus water saturation for Tensleep Sample A, calculated similar to example 3.30 shown in Figure 17. Although the curves are not as smooth as expected, the difference between vertical and horizontal relative permeabilities is obvious.

Task 3.0 - CO_2 FLOOD - FORMATION ALTERATION AND WELLBORE DAMAGE

OBJECTIVE

The work of this task is to establish criteria for susceptibility of Tensleep reservoirs to formation alteration resulting in a change in absolute or relative permeability and possible wellbore scale damage during CO_2 enhanced oil recovery. This advanced reservoir characterization technology will be used to optimize recovery efficiency. This task includes: (a) flow experiments on core material to examine the effects of CO_2 flooding on the alteration of the fluid and rock system; (b) examination of regional trends in water chemistry; (c) examination of local water chemistry trends at field scale and (d) chemical modeling of both the reservoir and experimental systems in order to scale-up the experiments to reservoir conditions.

INTRODUCTION

CO_2-flooding is an important technique for enhanced oil recovery (EOR). Since this technique has potential for EOR in the Bighorn and Wind River basins, Wyoming, it is indispensable to properly understand the effect of CO_2 treatment to scale formation and formation damage or enhancement in those oil fields.

Previous works describe the effects of CO_2 treatment to hydrocarbons and minerals in reservoirs. Monger and Fu (1987), Monger and Trujillo (1988), Wolcott et al. (1989) assessed asphaltene precipitation as a by-product of CO_2-oil interaction. Ross et al. (1981, 1982) and Sayegh et al. (1990) showed that permeability is enhanced due to carbonate cement dissolution by CO_2 injection through core-flooding experiments. However, only a few studies have focused on water-rock interaction caused by CO_2 treatment (Bowker and Shuler, 1991). The work of Task 3.0 has focused on laboratory chemical modeling and the use of CO_2-flooding laboratory experiments in order to predict formation alteration and scale formation in the Tensleep Formation in Bighorn and Wind River basins.

FORMATION WATER CHEMISTRY

Water Chemistry

Ninety-four water analyses for the Tensleep Formation have been obtained from the database of the Wyoming State Geological Survey, publications, and industrial sources. The waters which have been included in the study have a charge balance of ± 10%. The analyses include data of total dissolved solid (TDS), pH, Na^+, K^+, Mg^{2+}, Ca^{2+}, $SO4^{2-}$, Cl^-, and $HCO3^-$. The latitude and longitude were obtained for each well.

The TDS of the Tensleep Formation waters varies from 234 mg/l to 10,994 mg/l, which is much lower than that of sea water (35, 000 mg/l). NaCl-type solution has not been found which would be the expected original connate water in an eolian sediment flooded by seawater. These compositions indicate that the original formation waters were completely flushed out of the formation due to penetration of meteoric water and that reaction between rock and the meteoric water produced new formation water chemistry. The burial history analysis indicates that the Tensleep Formation experienced relatively shallow burial during its early history. Hence, pre-Laramide flushing and mixing of connate and meteoric water likely occurred. The current distribution of water chemistry, however, clearly shows a Laramide recharge pattern.

Figure 20 shows water chemistry of the Tensleep Formation waters in a Piper Diagram. This diagram permits the display of the cation and anion compositions of many samples in a single diagram, however, total dissolved solids are not shown (e.g., Freeze and Cherry, 1979). The diagram shows also the composition of sea water for comparison. Two types of water chemistry have been identified in Tensleep Formation water. One is rich in Ca^{2+}, Mg^{2+}, $SO4^{2-}$, and $HCO3^-$ and has very low Cl^- content, whereas the other has higher Cl^- and ($Na^+ + K^+$). Therefore, Type A and B waters are defined in terms of equivalent fraction of chloride, X_{Cl}, defined by:

$$X_{Cl} = M_{Cl} \,/\, (M_{Cl^-} + M_{SO4^{2-}} + M_{HCO3^-})$$

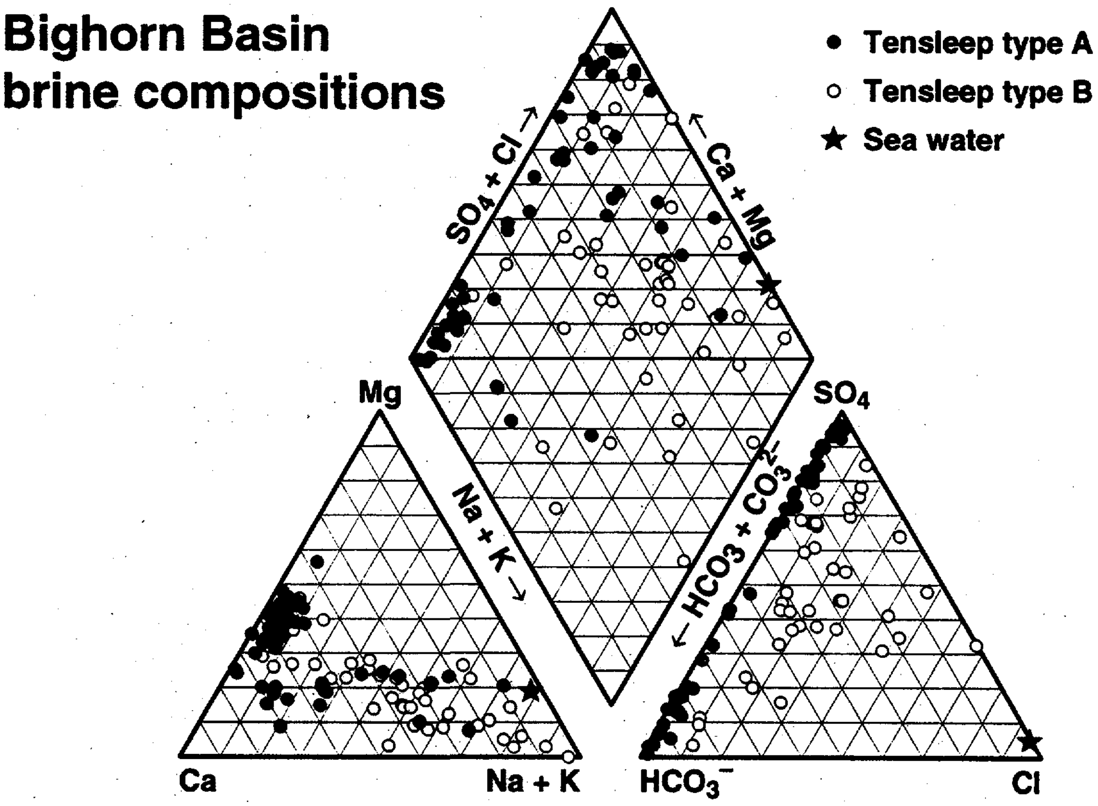

Figure 20. Chemical composition of Tensleep Formation waters (Piper Diagram).

where M_i is the concentration of i-th component in meq/l unit. According to this definition, Type A waters have X_{Cl} smaller than 0.05, whereas Type B waters have X_{Cl} greater than 0.05.

Figure 21 shows the relation between $[Ca^{2+} + Mg^{2+}]$ and $[SO_4^{2-} + HCO_3^-]$ for Type A waters. As seen in the figure, a good linearity is observed except for three data points having higher $SO_4^{2-} + HCO_3^-$ concentrations. Mankiewicz and Steidman (1979) demonstrated that the Tensleep Formation is cemented by anhydrite and dolomite in the eastern Bighorn basin. Therefore, water chemistry of Type A is probably controlled by dissolution/precipitation of anhydrite (and/or gypsum) and dolomite (and/or calcite). However, Type B waters do not show a good linearity between $[Ca^{2+} + Mg^{2+}]$ and $[SO_4^{2-} + HCO_3^-]$ as observed for Type A water. This is probably due to higher content of Cl^-.

Figures 22 and 23 show the distribution of wells which produced Type A and Type B waters, respectively, as well as the TDS range. The wells that produced Type A waters are distributed mainly along the northeast side of the Bighorn Basin, whereas Type B waters are distributed mainly along the southwest side of the basin. The high-TDS waters of both types are found along the perimeter of the basin, indicating that the basin bounding faults prevent penetration of meteoric water, as shown by Huntoon (1982a, b).

Chemical modeling

SOLMINEQ.88 (Kharaka et al., 1988) was used to calculate speciation of the water chemistries. Saturation index (*S.I.*) defined by:

$$S.I. = \log (IAP/K_{sp})$$

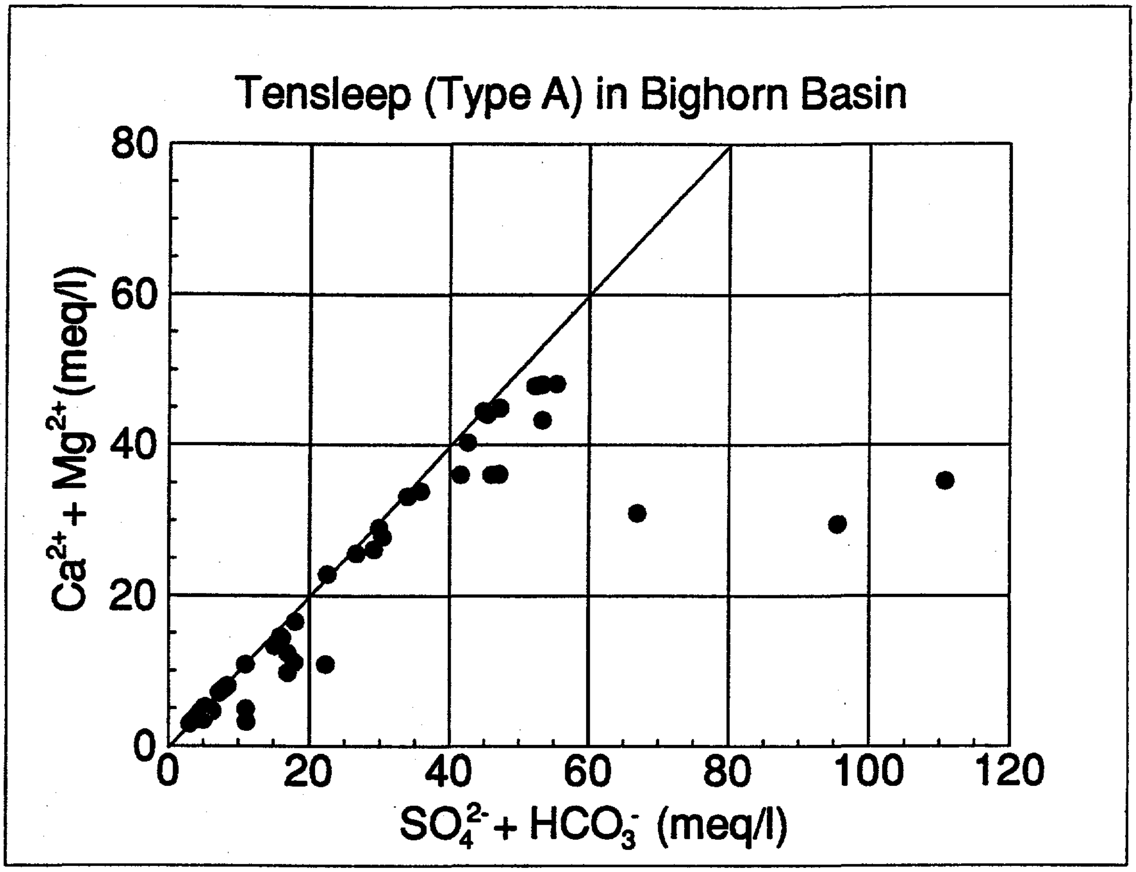

Figure 21. **$[Ca^{2+} + Mg^{2+}]$ vs. $[SO_4^{2-} + HCO_3^-]$ for Type A waters.**

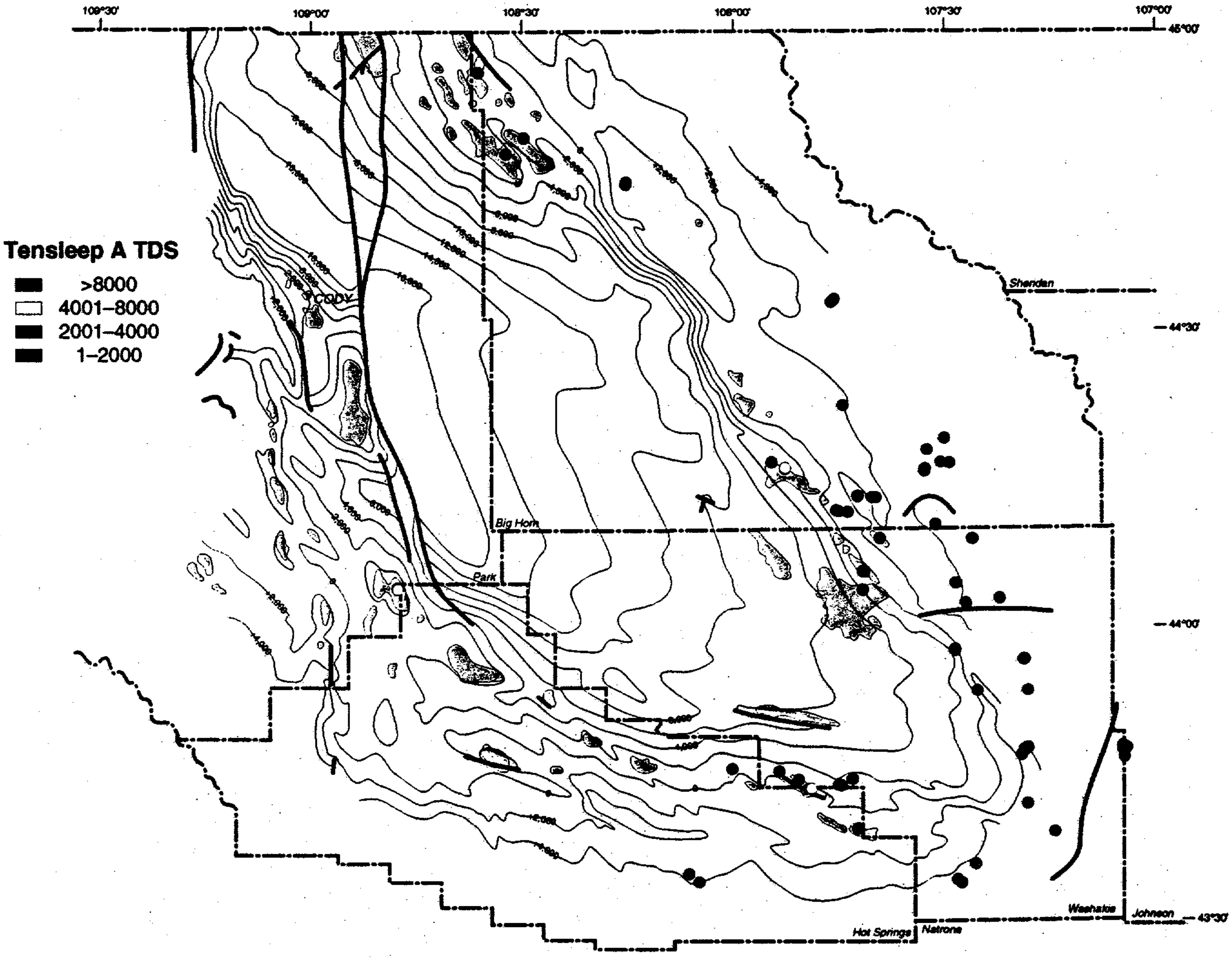

Figure 22. Distribution of Type A waters in the Bighorn basin. Contours and shaded areas show the top of the Permo-Pennsylvanian Phosphoria and Minnelusa Formations and Tensleep oil fields, respectively, (WGA, 1989).

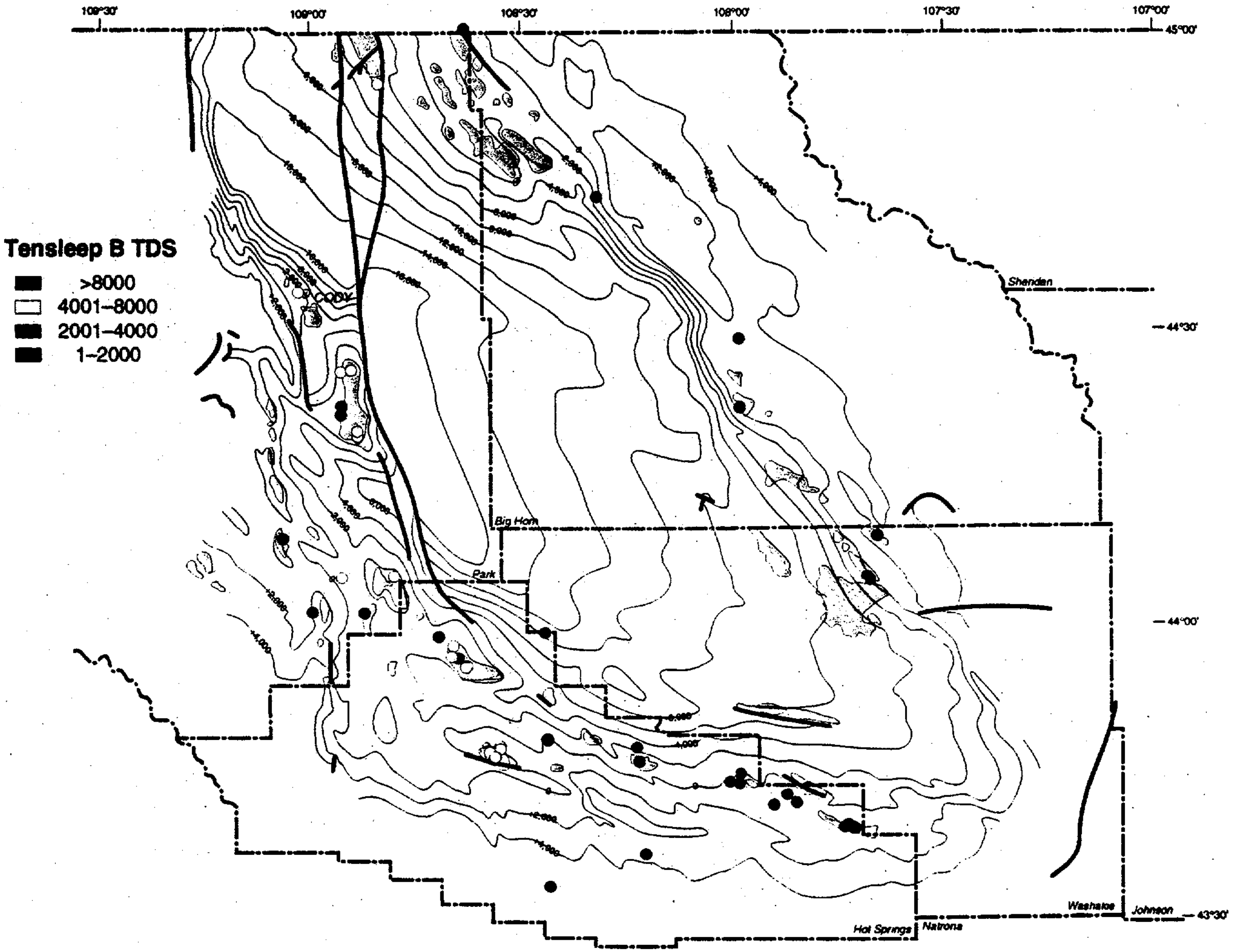

Figure 23. Distribution of Type B waters in the Bighorn basin. Contours and shaded areas are the same as in Figure 22, (WGA, 1989).

was calculated for sulfate and carbonate minerals using the results of speciation. Where *IAP* and K_{sp} are ion activity product and solubility product for a mineral. For example, since dissolution of anhydrite is expressed by:

$$CaSO_4 = Ca^{2+} + SO_4^{2-}$$

saturation index of anhydrite is given by the following equation:

$$S.I.\ (anhydrite) = \log [\ aCa2+\ a_{SO4}^{2-} / K_{sp}\ (anhydrite)\ ]$$

the saturation index of a mineral is 0 when the solution is in equilibrium with the mineral; positive and negative values indicate super- and undersaturation, respectively. Table 4 lists values of K_{sp} of sulfate and carbonate minerals. We changed K_{sp} for dolomite to the value shown in Table 4, because the value in the database of *SOLMINEQ.88* is almost one order smaller than that generally accepted (Hsu, 1967; Langmuir, 1971; Plummer and Busenberg, 1982; Drever, 1988).

Table 4. Solubility product of sulfate and carbonate minerals at 80^{o}C and 165.5 bars.

anhydrite	-4.88	calcite	-8.83
gypsum	-4.77	aragonite	-8.72
barite	-9.45	dolomite	-18.41
celestite	-6.62		

Figures 24 and 25 show the relation between TDS and saturation index of anhydrite and gypsum of both types, respectively. Both figures show that the degree of saturation of these two minerals is a function of TDS. At low TDS, no difference in saturation index of both types can be seen. However, as TDS increases, saturation index of Type A increases at a higher rate than that of Type B, and it becomes saturated with respect to gypsum at about 3,500 mg/l of TDS. However, Type B waters are not saturated with respect to gypsum even at higher TDS, whereas they show a similar trend to that of Type A. This is

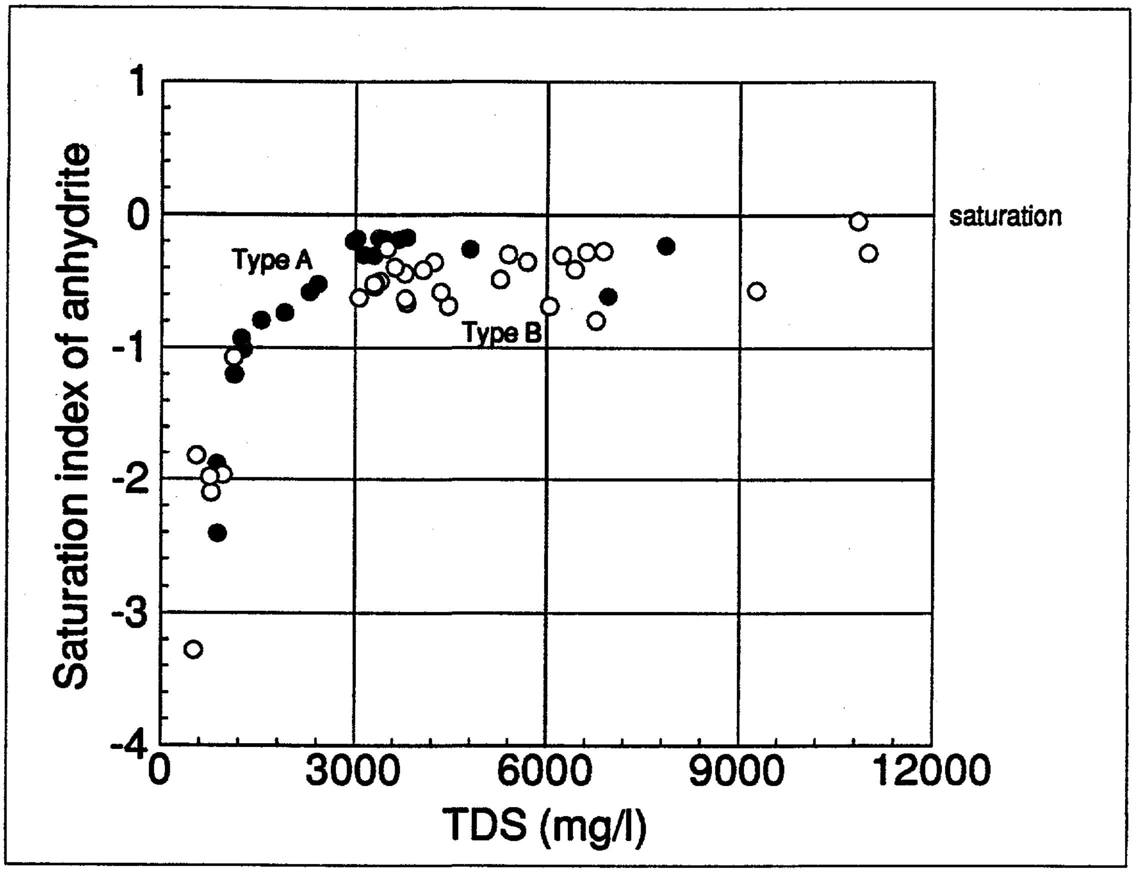

Figure 24. Saturation index of anhydrite vs. total dissolved solid (TDS).

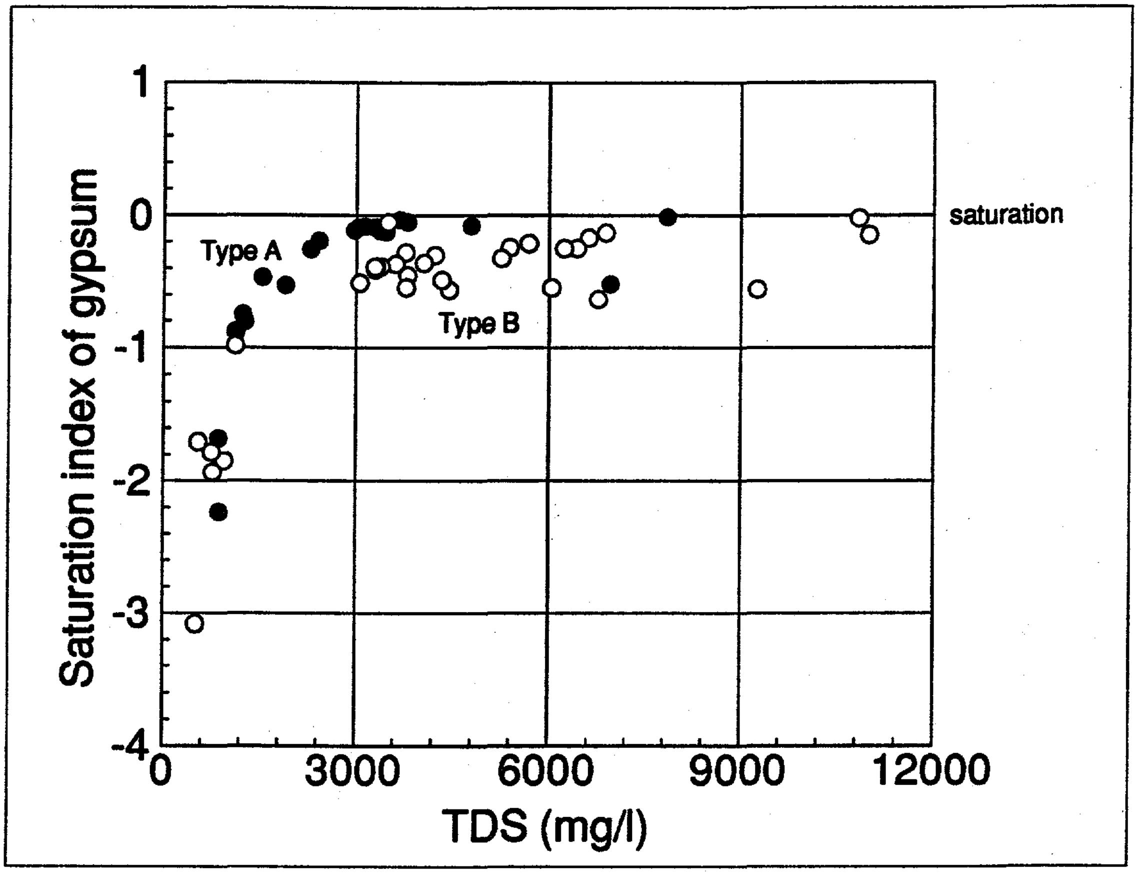

Figure 25. Saturation index of gypsum vs. total dissolved solids (TDS).

probably due to the effect that higher ionic strengths have in decreasing the activities of Ca^{2+} and SO_4^{2-}.

Waters of both types are highly supersaturated with respect to dolomite. Langmuir (1971) showed that waters from Paleozoic carbonate rocks are almost saturated with respect to dolomite by using field pH and taking into account ion pairs of $CaSO_4^{o}$, $MgSO_4^{o}$, and $MgHCO_3^{+}$ in speciation, whereas previous studies showed that similar waters are highly saturated with respect to dolomite (e.g., Barnes and Back, 1964; Holland et al., 1964; Back and Hanshaw, 1970). *SOLMINEQ.88* contains the thermodynamic database of the ion pairs which Langmuir (1971) considered. However, it is not clear if the pH of the waters contained in our database were measured immediately after sampling. Thus, accurate pH values are indispensable to calculate exact saturation index of carbonates.

CO_2-CORE FLOODING EXPERIMENT

Materials

Three subsurface cores from the Tensleep Formation in the Oregon Basin oil field were used for the first experiment. The dimensions of cores are 1.5 inches in diameter and 3.0 inches in length. Cores for experimental use were obtained from conventional 4 inch diameter cores by drilling approximately parallel to lamination. These cores are considerably cemented by dolomite. Physical data of porosity, pore volume, and air permeability of these cores measured before the experimental run are listed in Table 5 as well as those after run.

The nutrient solution was prepared by dissolving reagents $CaSO_4$, $MgSO_4$, and Na_2SO_4 into distilled water. This solution has a simplified composition of Type A formation water and is adjusted to be equilibrated with respect to anhydrite at experimental P-T conditions ($80^{o}C$ and 165.5 bars). The chemical composition of the nutrient solution is shown in Table 6.

Table 5. Physical properties of core samples before and after run.

core	depth (ft)	pore volume (cc)		porosity (%)		air permeability (md)	
		before	after	before	after	before	after
1	3287.35	9.94	9.87	11.7	11.6	97.24	99.92
2	3286.70	8.04	7.95	9.4	9.3	56.92	71.95
3	3287.90	7.07	7.05	8.3	8.3	53.53	72.55

Table 6. Chemical composition of the nutrient solution (mg/l).

Na	194
Mg	122
Ca	447
SO_4	1950

Apparatus and Run

The experiment was carried out at the Petroleum Technology Center, Marathon Oil Company, Littleton, CO. Figure 26 contains a schematic diagram of the experimental apparatus used. Core samples were wrapped with teflon sheet and aluminum foil. These wrapped cores were placed into a rubber tubing and both sides of the tubing were tightly attached to stainless steel core-ends with tubing clamps. This core assemblage was placed in the core holder (high pressure vessel) and water was injected into the free space in the vessel. Then, N_2 gas was introduced into the tank connected to the pressure vessel to obtain an overburden pressure of 4,000 psi. This overburden pressure ensures a tight fit between the rubber tubing and the outside cores, thus preventing the passing of solution through the space between rubber tubing and outside of cores.

About 400ml of nutrient solution was injected into cylindrical reservoirs (500 ml volume) from the bottom side and then CO_2 gas was injected into them from the same side to obtain pressure of about 2,000 psi. After the temperature of the system reached $80^{o}C$, CO_2-pressure was exactly adjusted to 2,400 psi by releasing a small aliquot of nutrient solution. Constancy of CO_2 pressure suggested that equilibrium between CO_2 and the nutrient solution was obtained. A Ruska pump was used to send mineral oil into the upper

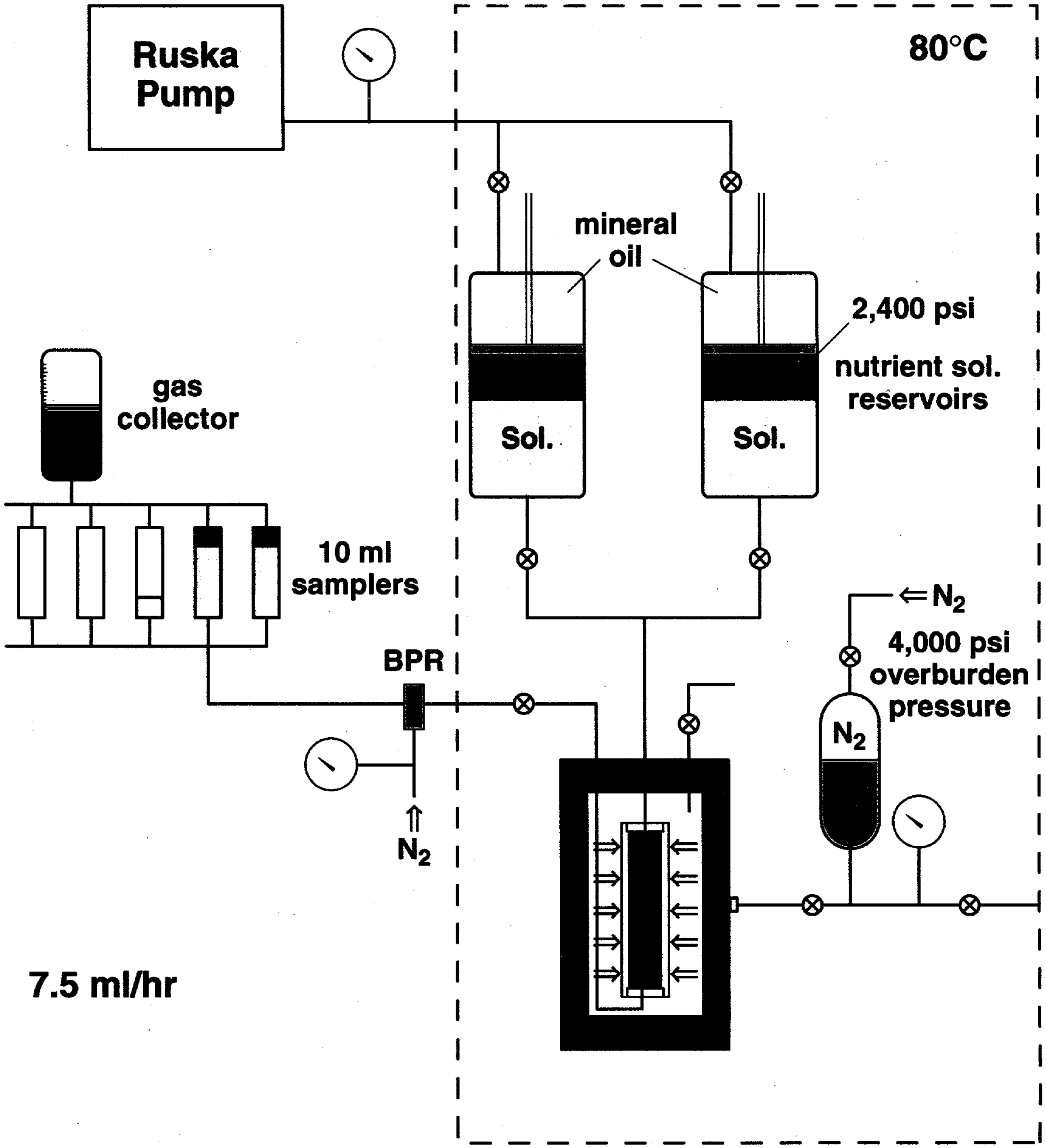

Figure 26. Schematic diagram of the core-flooding apparatus.

part of the separator of the reservoirs, displacing nutrient solution equilibrated with CO_2 gas into cores.

Effluent solution was collected into cylindrical samplers after passing through the back-pressure regulator. The pressure for the back-pressure regulator was set to 20 psi lower than that of nutrient solution reservoirs throughout the run. The flow rate of the nutrient solution was set to 7.5 ml/h. Degassed CO_2 out of sample solutions was collected into a gas collector and the volume was measured. The duration of this first run was 60 hours.

Analyses

Three sample solutions were mixed together to collect a 30ml sample. After mixing solutions, the pH of the mixtures were measured using a combination pH electrode. Then, 1N HCl was added into the sample solutions to keep iron in solution. However, the first five samples were filtered before adding HCl and some $Fe(OH)_3$ precipitate was removed out of the solutions. Therefore, Fe content of these solutions should be of minimum values. Concentrations of Ca, Mg, Fe, Na, Al, Ba, Sr, Si, SO_4 were measured by ICP, and K was measured by atomic absorption spectrometry at the University of Wyoming (by Dr. S. Boese).

Speciation of solutions

SOLMINEQ.88 (Kharaka et al., 1988) was used to calculate speciation of solutions. Degassed CO_2 was taken into account to calculate *in-situ* pH values in these calculations.

Results and Discussion

Figure 27 shows changes of pH and silica with time. The first sample had much higher silica content (0.86 mmol/l) and pH value (4.2) compared with the nutrient solution. However, silica content decreased with time. The rate of decrease was rapid for the first 20

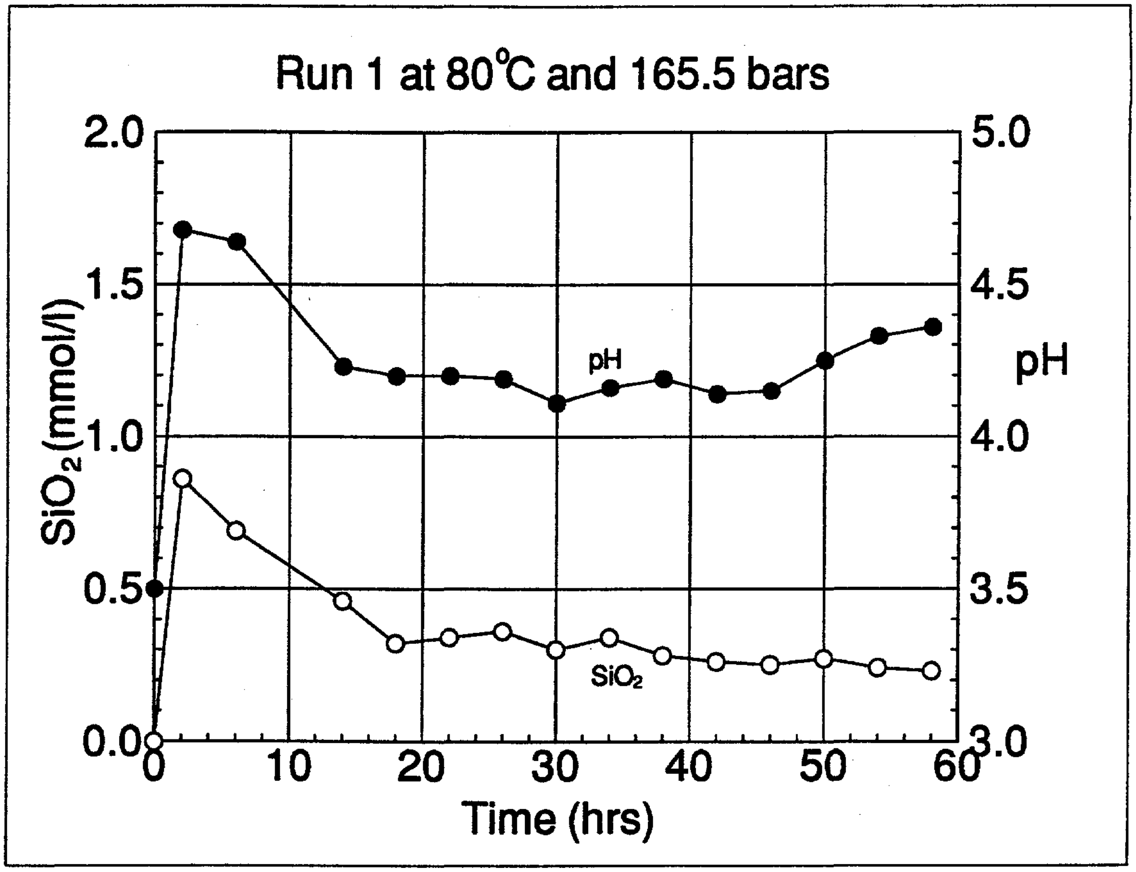

Figure 27. Change of pH and silica with time.

hours, whereas the rate became slower after t = 20 hrs. The other components such as Na, K, Sr showed quite similar concentration changes with time to that of silica. The solution pH became lower with time and obtained a steady state (pH = 4.2) after t = 16 hrs. However, pH rose again at the end of run (after t = 48 hrs). These changes suggest that H^+ reacted with silicate(s) to form secondary phases, such as clay minerals at the early stage of the run.

Figure 28 shows the concentration change of Ca^{2+}, Mg^{2+}, and $SO4^{2-}$ with time. Mg^{2+} and $SO4^{2-}$ contents of the first sample were 28 and 15% less than those of the nutrient solution. Mg^{2+} content, however, increased with time and the final solution contained 12% more Mg^{2+} compared with nutrient solution. $SO4^{2-}$ concentration change was more complex. However, generally speaking, $SO4^{2-}$ content gradually decreased with time and the final solution contained 20% less $SO4^{2-}$ compared with the original solution. Ca^{2+} content rose up 31% in the first sample compared with the nutrient solution and then decreased rapidly in the second and third samples, whereas subsequent change was slow. The final concentration was 90% of the original one.

Quick chemical change in the early stage of the run may be due to reactions of hydrolysis of silicates and formation of Mg-bearing clay mineral(s), which were observed in many experimental works on volcanic rock-sea water interactions (e.g., Bischoff and Dickson, 1975; Mottl and Holland, 1978; Hajash and Chandler, 1981; Seyfried and Bischoff, 1981, Shiraki et al., 1987). However, subsequent increase in Mg^{2+} and slow decrease in Ca^{2+} and $SO4^{2-}$ are consistent with the results of Bowker and Schuler (1991) and suggest dissolution of dolomite and precipitation of anhydrite.

Figures 29 and 30 show change of saturation index with time of sulfate and carbonate minerals, respectively. In spite of a complex pattern of sulfate concentration change (Fig. 28), the saturation index of all sulfate minerals are constant through the run. Solutions were slightly undersaturated with respect to anhydrite and gypsum. Errors in saturation index for anhydrite are within diameters of the plotted symbols. As

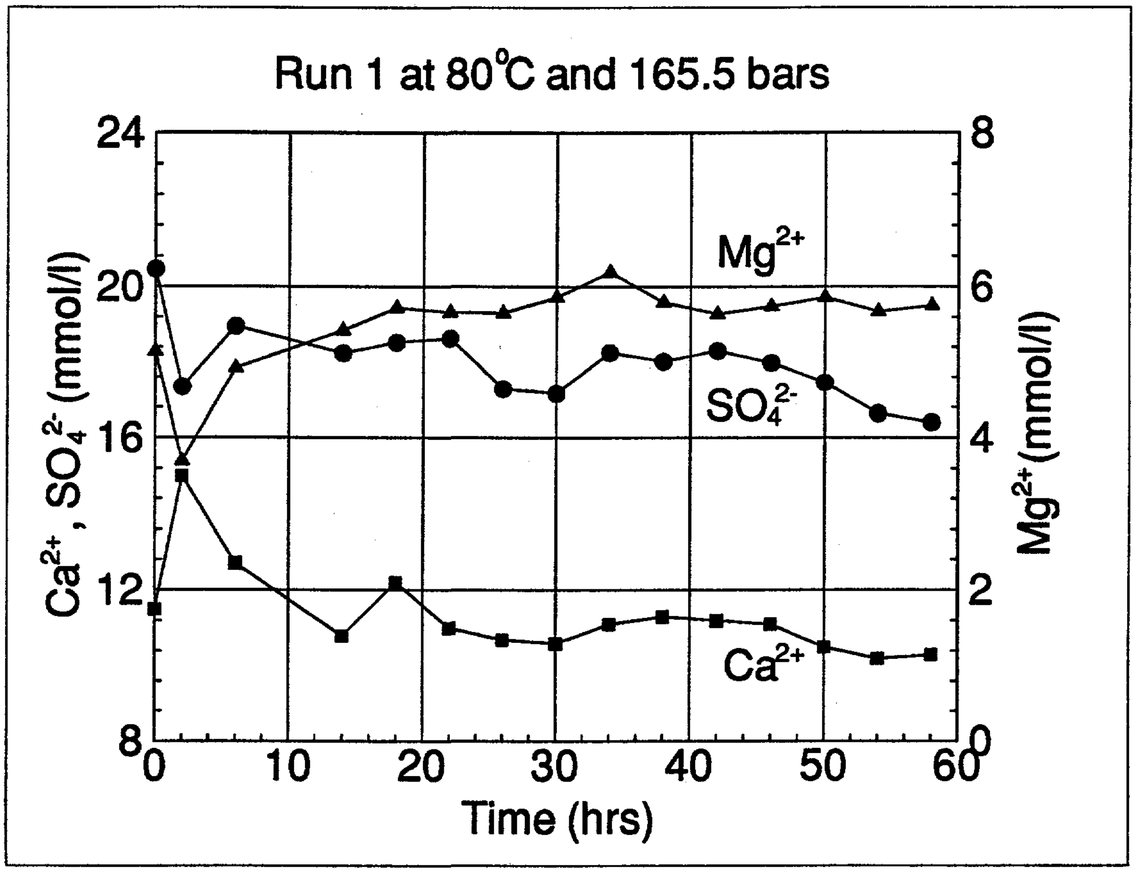

Figure 28. Change of Ca^{2+}, Mg^{2+}, and SO_4^{2-} with time.

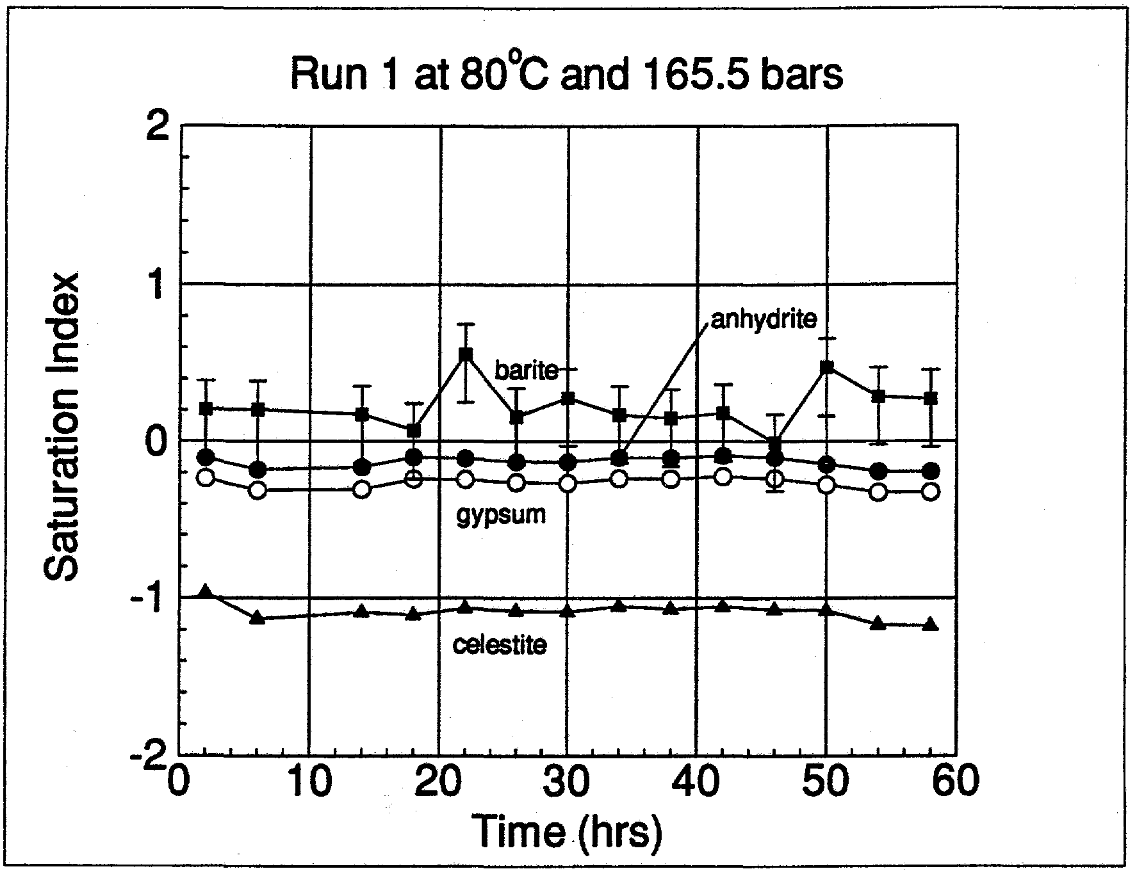

Figure 29. Saturation index of sulfates vs. time.

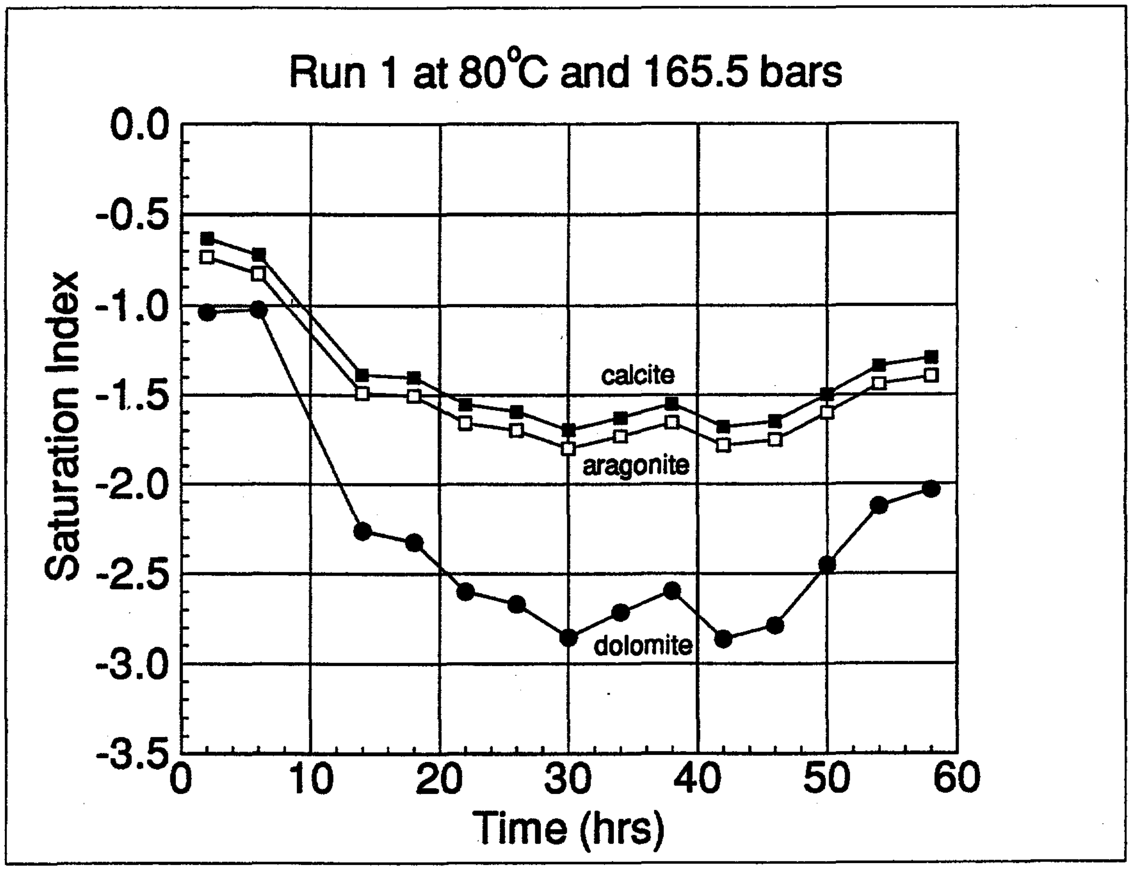

Figure 30. Saturation index of carbonates vs. time.

concentrations of Ca^{2+} and SO_4^{2-} decreased, anhydrite probably precipitated to keep the degree of saturation of anhydrite slightly lower than saturation value. Because the Ba^{2+} content of solutions was close to the detection limit of ICP, the analytical error reached ±100% in some data. Figure 29 shows error bars for saturation index of barite by assuming ± 50% and ± 2% errors for Ba^{2+} and SO_4^{2-}, respectively. The figure shows that the solution is equilibrated with respect to barite within error throughout the run except for two solutions. This fact suggests barite scale can be formed as Ba^{2+} is dissolved into solution from the mineral phases.

The degree of saturation of carbonate minerals changed considerably with time, although solutions were undersaturated with respect to these minerals throughout the run. The saturation index of dolomite was - 1.0 at the early stage of the run, then dropped to -2.85 at t = 30 hrs and then rose to -2.03 at the end of the run. Patterns of calcite and aragonite S.I. are similar to that of dolomite, whereas the degree of undersaturation is smaller.

Undersaturation of carbonate minerals suggests that scale of these minerals will be hard to form under the present P-T conditions (i.e., reservoir conditions). However, as CO_2 waters move to production wells in the fields, scale formation might occur due to pressure decrease, that is, degassing of CO_2. In that case, calcite or aragonite should precipitate rather than dolomite, because nucleation of dolomite is very slow (e.g., Blatt et al., 1979; Busenberg and Plummer, 1982). Precipitation of calcite vs. aragonite depends on Mg/Ca ratio of the precipitating solution and crystallization rate (Folk, 1974; Given and Wilkinson, 1984; Burton, 1993).

CONCLUSIONS

Two types of water chemistries (Type A and B) have been identified in the Tensleep Formation waters. These data suggest episodes of complete flushing of the original formation water, dissolution and precipitation of authigenic minerals, and communication with other NaCl-type formation waters. Chemical modeling of these waters suggests that saturation of the sulfates (anhydrite and gypsum) is a function of total dissolved solid (TDS) and that Type A waters are saturated with respect to gypsum at around 3,500 mg/l TDS, whereas Type B water are undersaturated with respect to this mineral even at higher TDS.

A core-flooding experiment was carried out at 80^{o}C and 165.5 bars ($P_{CO2} = P_{total}$) using core samples from the Tensleep Formation, Oregon Basin oil field and synthetic formation water of Type A. The results show that solutions were equilibrated with respect to barite and the possibility of the formation of barite scale. Solutions were undersaturated with respect to carbonate minerals (dolomite, calcite, and aragonite) throughout the run, suggesting that carbonate scales will not form prior to CO_2 pressure drop within the production tubing and perforations.

FUTURE PLANS

Through the first CO_2 core-flooding experiment, we did not have any serious technical problems and thus, the first experiment was successful. Therefore, we plan to run three more experiments in the next year for more accurate prediction of formation damage and scale formation in Bighorn and Wind River basins.

In the second run, we will run a similar experiment to the first run, however a different water chemistry (Type B) will be adopted. Duration of the second run should be longer in order to observe the long-term change of saturation index of minerals. In the third and fourth runs, we will place petroleum in the experimental systems. The experiments on rock-oil-water-CO_2 systems can provide us more exact information on formation damage in the natural systems. Comparison of the results of these runs with those of first two runs will enable us to assess the effect of oil-CO_2 interaction on formation damage and scale formation.

Collection of water chemistry of the Tensleep Formation waters is in progress. More data on water chemistry will enable us to predict scale formation accurately in the Formation as well as improve the experimental design. The sampling of formation waters will focus on the measurement of the accurate water chemistry, in particular, pH values.

TASK 4.0 - PROJECT MANAGEMENT AND TECHNICAL TRANSFER

OBJECTIVES

This task incorporates efforts to achieve a high level of success in this interdisciplinary project. This administrative task provides for effective coordination and integration of the project's research tasks. The program manager is responsible for ensuring that the task workers meet on a frequent and regular basis to exchange information and discuss results. The program manager is responsible for the coordination and timely reporting of results to its Industry Advisor/Mentors, the Department of Energy, and the scientific and engineering communities.

The project reached full staffing in the third quarter. The Industrial Advisor/Mentors have been consulted through correspondence and phone conversations. The entire research group has met on a regular basis to review the project's direction. The project personnel and project organization (Fig. 31) has shifted slightly. Dr. L.K. Smith, a coauthor of the proposal, left the project briefly but was retained in the capacity of an Industrial Advisor/Mentor, she has now returned to the Institute. Dr. Smith will be involved in Tasks 3.0 and 4.0.

Two papers describing the first results of this research have been accepted for presentation at the AAPG annual meeting in Houston, March 8, 1995. The abstracts and letters of acceptance can be found in the Appendix.

The second year will see a strengthening of the Task 2.0 effort. This will be accomplished through the addition of engineering personnel.

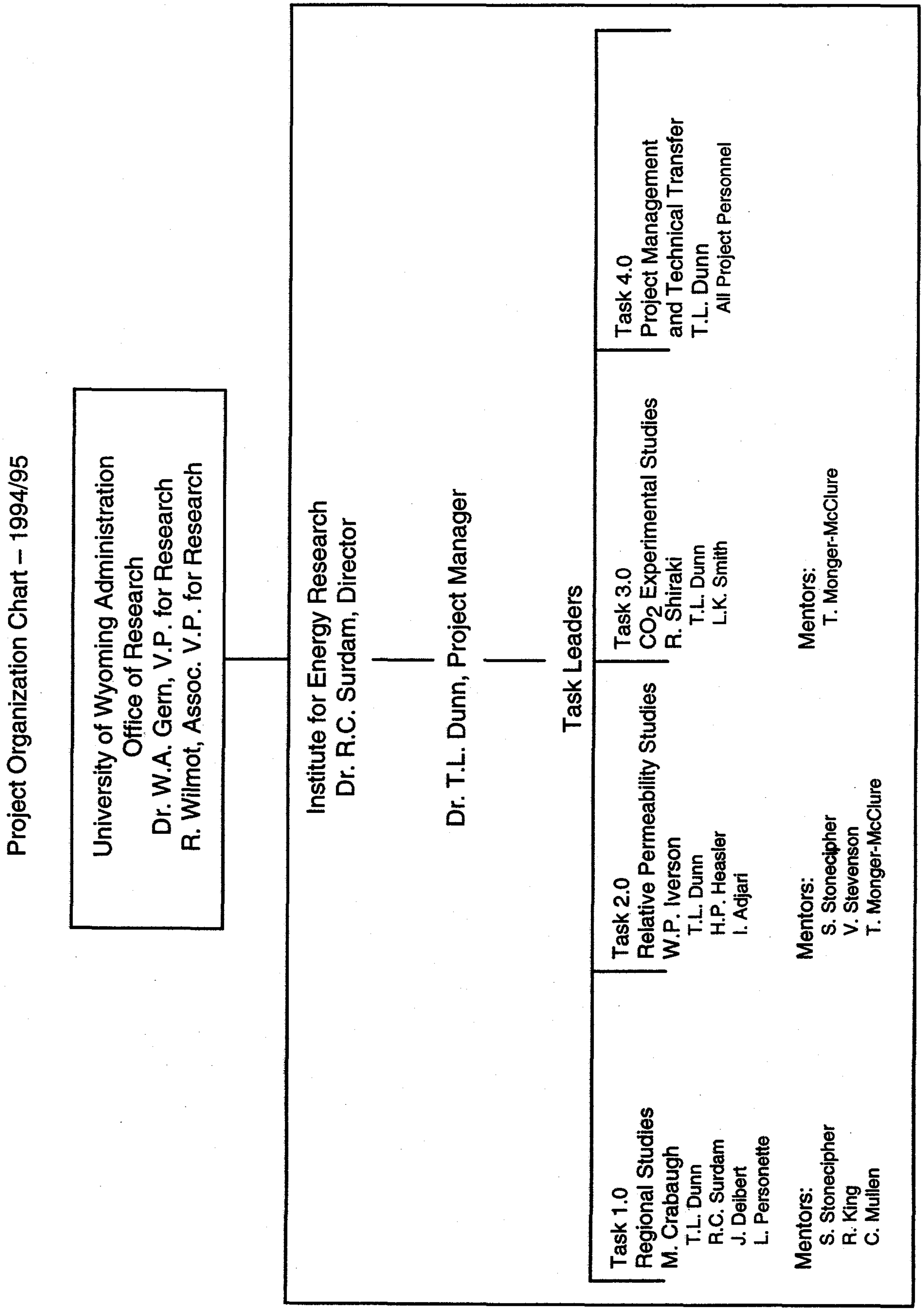

Figure 31. Project Organizational Chart, 1994/95.

REFERENCES

Agatston, R.S., 1952, Tensleep Formation of the Bighorn Basin; Wyoming Geological Association Guidebook, Seventh Annual Field Conference, p. 44-48.

Agatston, R.S., 1954, Pennsylvanian and Lower Permian of northern and eastern Wyoming; American Association of Petroleum Geologists Bulletin, v. 38, p. 508-583.

Andrews, S. and Higgins L.S., 1984, Influence of depositional facies on hydrocarbon production in the Tensleep sandstone, Big Horn Basin, Wyoming; A working hypothesis. Wyoming Geological Association Guidebook, Thirty-fifth Annual Field Conference, p. 183-197.

Back, W. and Hanshaw, B. B. (1970) Comparison of chemical hydrogeology of the carbonate peninsulas of Florida and Yucatan. *Jour. Hydrol.* 10, 330-368.

Barnes, I. and Back, W. (1964) Dolomite solubility in ground water. *U.S. Geol. Surv. Prof. Paper,* 475-D, 179-180.

Bischoff, J. L. and Dickson, F. W. (1975) Seawater-basalt interaction at $200^{\circ}C$ and 500 bars: Implication for origin of sea-floor heavy metal deposits and regulation of seawater chemistry. *Earth Planet. Sci. Lett.* 25, 385-397.

Blatt, H., Middleton, G., and Murray, R. (1982) Origin of sedimentary rocks. Prentice Hall, New Jersey, p.782.

Bowler, K. A. and Schler, P. J. (1991) Carbon dioxide injection and resultant alteration of the Weber sandstone, Rangely Field, Colorado. *Amer. Assoc. Petrol. Geol. Bull.* 75, 1489-1499.

Brainerd, A.E., and Keyte I.A., 1927, New faunal evidence from Tensleep Formation; Journal of Paleontology v.1, p. 173-174.

Branson, C.C., 1939, Pennsylvanian formations of central Wyoming; Geological Society of America Bulletin, v.50, p. 1199-1226.

Burton, E. A. (1993) Controls on marine carbonate cement mineralogy: review and reassessment. *Chem. Geol.* 105, 163-179.

Busenberg, E and Plummer, L. N. (1982) The kinetics of dissolution of dolomite in CO_2-H_2O systems at 1.5 to $65^{\circ}C$ and 0 to 1 atm P_{CO_2}. *Amer. Jour. Sci.,* 282, 45-78.

Crabaugh, M.C., 1994, Controls on Accumulation in Modern and Ancient Wet Eoian Systems; Ph.D. dissertation, University of Texas at Austin, Austin, Texas, 150p.

Crowell, J.C., and Frakes L.A., 1972, Late Paleozoic galciation: Part V, Karroo Basin, South Africa; Geological Society of America Bulletin, v. 83, p. 2887-2912.

Drever, J. I. (1988) The geochemistry of natural Waters. Prentice Hall, New Jersey, p.437.

Falk, R. and Land, L. S. (1975) Mg/Ca ratio and salinity: two controls over crystallization of dolomite. *Amer. Assoc. Petrol. Geol. Bull.* 59, 60-68.

Frank, A.F., 1994, Models for Airflow Velocity Profiles in Natural settings Accounting for Atmospheric Conditions and Secondary Flow, Ph.D. dissertation, University of Texas at Austin, Austin, Texas, 120p.

Freeze, R. A. and Cherry, J. A. (1979) Groundwater, Princeton Hall, New Jersey, p. 604.

Given, R. K. and Wilkinson, B. H. (1985) Kinetic control of morphology, composition, and mineralogy of abiotic sedimentary carbonates. *Jour. Sedimet. Petrol.* 55, 109-119.

Hajash, A. and Chandler, G. W. (1981) An experimental investigation of high temperature interaction between seawater and rhyolite, andesite, basalt and peridotite. *Contrib. Mineral. Petrol.* 78, 240-254.

Henbest, L.G., 1956, Foraminifera and correlation of the Tensleep Sandstone of Pennsylvanian age in Wyoming; Wyoming Geological Association Guidebook, Eleventh Annual Field Conference, p. 58-63.

Henbest. L.G., 1954, Pennsylvanian formaminifera in Amsden Formatin and Tensleep Sandstone, Montana and Wyoming. Billings Geological Society Guidebook, Fifth Annual Field Conference, p.50-53.

Hoare, R.D., and Burgess J.D., 1960, Fauna from the Tensleep Sandstone in Wyoming; Journal of Paleontology, v. 34, p. 711-716.

Holland, H. D., Kirssipu, T.V., Huebner, J. S., and Oxburg, U. M. (1964) On some aspects of the chemical evolution of cave waters. *Jour. Geol.* 72, 36-67.

Hsu, K. J. (1963) Solubility of dolomite and composition of Florida ground waters. *Jour. Hydrol.* 1, 288-310.

Huntoon, P. W. (1985a) Fault severed aquifers along the perimeters of Wyoming artesian basins. *Ground Water* 23, 176-181.

Huntoon, P. W. (1985b) Rejection of recharge water from Madison aquifer along eastern perimeter of Bighorn artesian basin, Wyoming. *Ground Water* 23, 345-353.

Kerr, D.R., 1989, Sedimentology and stratigraphy of Pennsylvanian and Lower Permian strata (Upper Amsden Formation and Tensleep Sandstone) in north-central Wyoming. Ph.D; Thesis, University of Wisconsin, Madison, Wisconsin, 382p.

Kerr, D.R., and Dott, R.H., 1988, Eolian dune types preserved in the Tensleep Sandstone (Pennsylvanian-Permian), north-central Wyoming; Sedimentary Geology, 56, 383-402.

Kerr, D.R., Wheeler, D. M., Rittersbacher, D.J., and Horne J. C., 1986. Stratigraphy and sedimentology of the Tensleep Sandstone (Pennsylvanan and Permain), Bighorn Mountains, Wyoming; Wyoming Geological Association Earth Science Bulletin, v. 19, pt. 2, p. 61-77.

Kharaka, Y. K., Gunter, W. D., Aggarwal, P. K., Perkins, E. H., and De Braal, J. D. (1988) SOLMINEQ.88: A computer program code for a geochemical modeling of water-rock interactions. *U.S. Geol. Surv. Water Res. Investigation Rep.* 88-4227.

Kocurek G., and Havholm, K., 1993, Eolian sequence stratigraphy--a conceptual framework; in P. Weimer and H. Posamentier (eds) Recent Advances in and Applications of Siliciclastic Sequence Stratigraphy, American Association of Petroleum Geologists, Memoir 58, p.393-409.

Kocurek, G., 1988. First-order and super bounding surfaces in eolian sequences--bounding surfaces revisited, in Kocurek, G., (ed.), Late Paleozoic and Mesozoic Eolian Deposits of the Western Interior of the United States; Sedimentary Geology, 56, 193-206.

Langmuir, D. (1971) The geochemistry of some carbonate ground waters in central Pennsylvania. *Geochim. Cosmochim. Acta* 35, 1023-1045.

Mankiewicz, D and Steidtmann, J. R. (1979) Depositional environments and diagenesis of the Tensleep sandstone, eastern Big Horn basin, Wyoming. *Soc. Econ. Paleontol. Mineral., Spec. Publ.* 26, 319-336.

Mankiewicz, D., and Steidtmann J.R., 1979, Depositional environments and diagenesis of the Tensleep Sandstone, eastern Big Horn Basin, Wyoming; in P.A. Scholle, and P.R. Schluger, eds., Aspects of Diagenesis. Society of Economic Paleontologists and Mineralogists Special Publication 26, p. 319-336.

Monger, T. G. and Trujillo, D. E. (1986) Organic deposition during and rich-gas flooding. *Soc. Petrol. Eng. SPE Paper* 18063, 63-73.

Monger, T.G. and Fu, J. C. (1981) The nature of CO_2-induced organic deposition. *Soc. Petrol. Eng. SPE Paper* 16713, 147-159.

Mottl, M. J. and Holland, H. D. (1978) Chemical exchange during hydrothermal alteration of basalt by seawater. *Geochim. Cosmochim. Acta* 42, 1103-1115.

Paola, C. and Borgman, L. 1991. Reconstructing random topography from preserved stratification; Sedimentology, 38, 553-565.

Parrish J.T., and Peterson, F., 1988. Wind directions predicted from global circulation models and wind directions determined from eolian sandstones of the western United States - A comparison; in Kocurek, G., (ed.), Late Paleozoic and Mesozoic Eolian Deposits of the Western Interior of the United States. Sedimentary Geology, 56, 261-282.

Peterson, F., 1988, Pennsylvanian to Jurassic eolian transportation systems in the western United States; in G. Kocurek (ed.), Late Paleozoic and Mesozoic Eolian Deposits of the Western Interior of the United States. Sedimentary Geology, 56, 207-260.

Ramsbottom, W.H.C., 1979, Rates of transgression and regression in the Carboniferous of NW Europe; Geological Society of London Journal, v. 136, p. 147-153.

Rhodes, F.H.T., 1963, Conodonts from the topmost Tensleep Sandstone of the eastern Big Horn Mountains, Wyoming; Journal of Paleontology, v. 37, p. 401-408.

Ross, G. D., Todd, A. C., and Tweedie, J. A. (1981) The effect of simulated CO_2 flooding on the permeability of reservoir rocks. *in* F. J. Fayer (ed), Enhanced Oil Recovery Developments in Petroleum Science, 13, 351-366.

Ross, G. D., Todd, A. C., Tweedie, J. A., and Will, A. G. S. (1982) The dissolution effects of CO_2-brine systems on the permeability of U.K. and North Sea calcareous sandstones. *Soc. Petrol. Eng./Dept. of Energy Paper* 10685, 4-7.

Rubin, D.M. and Humter, R.E., 1983, Reconstructing bedform assemblages from compound cross-bedding; in, Brookfield, M.E., and Ahlbrandt, T.S., (eds). Eolian Sediments and Processes. Developments in Sedimentology, 38, Elsevier, Amsterdam, 407-427.

Rubin, D.M., 1987, Cross-bedding, Bedforms and Paleocurrents; Society of Economic Paleontologists and Mineralogists Concepts in Geology, 1, 187p..

Sayegh, S. G., Krause, F. F., Girard, M., and DeBree, C. (1990) Rock/fluid interactions of carbonated brines in a sandstone reservoir: Pembina Cardium, Alberta, Canada. *Soc. Petrol. Eng. Formation Evaluation, Dec.*, 399-405.

Scotese, C.R., Bamback, R.K., and Barton, C., Van der Voo, R. and Ziegler, A.M., 1979, Paleozoic base maps; Journal of Geology, v. 87, p.217-277.

Seyfried, W. E. and Bischoff, J. L. (1981) Experimental seawater-basalt interaction at 300°C, 500 bars, chemical exchange, secondary mineral formation and implications for the transport of heavy metals. *Geochim. Cosmochim. Acta* 45, 123-134.

Shiraki, R., Sakai, H., Endoh, M., and Kishima, N. (1987) Experimental studies on rhyolite- and andesite-seawater interactions at 300°C and 1000 bars. *Geochem. Jour.* 21, 139-148.

Thomas, L.E., 1965, Sedimentation and structural development of the Big Horn Basin. American Association of Petroleum Geologists Bulletin, v. 49, p. 1867-1877.

Vail, P.R., Mitchum, R.M., and Thompson III, S., 1977, Seisic stratigraphy and global changes of sea level, Part 4 - Global cycles of relative changes of sea level, in Payton, C.E., ed., Seismic stratigraphy- Applications to hydrocarbon exploration; American Assocation of Petroleum Geologists, p. 83-97.

Verville, G.J., 1957, Wolfcampian fusulinids from the Tensleep Sanstone in the Big Horn Mountains, Wyomings; Journal of Paleontology, v. 31, p. 349-352.

Verville, G.J., Sanderson, G.A., and Rea, B.D., 1970, Missourian fusulinids from the Tensleep Sanstone, Bighorn Mountains, Wyoming; Journal of Paleontology, v. 44, p. 478-479.

Wanless, H.R., and Shepard, F.P., 1936, Sea level and climatic changes related to late Paleozoic cycles; Geological Society of America Bulletin, v. 47, p. 1176-1206.

Willhite, G. Paul, 1986, Waterflooding, Society of Petroleum Engineers Textbook Series v. 3, 326p.

Wheeler, D., 1986, Stratigraphy and sedimentology of the Tensleep Sandstone, southeast Bighorn Basin, Wyoming; Unpublished Masters Thesis, Colorado School of Mines, Golden, Colorado, 169p.

Wolcott, J. M., Monger, T. G., Sassen, R. and Chinn, E. W. (1989) The effects of CO_2 flooding on reservoir mineral properties. *Soc. Petrol. Eng. SPE Paper* 18467, 101-110.

Wyoming Oil and Gas Fields Symposium Bighorn and Wind River Basns, 1989, Oil and Gas Field Symposium Conference, Wyoming Geological Association, 555p.

☆U.S. GOVERNMENT PRINTING OFFICE: 1995 - 660-029/20027